





RESEARCH ARTICLE | JUNE 23 2025

Wavepacket and reduced-density approaches for high-dimensional quantum dynamics: Application to the nonlinear spectroscopy of asymmetrical light-harvesting building blocks

Joachim Galiana  ; Michèle Desouter-Lecomte  ; Benjamin Lasorne  



J. Chem. Phys. 162, 244102 (2025)

<https://doi.org/10.1063/5.0270440>



Articles You May Be Interested In

Excitation energy transfer and vibronic relaxation through light-harvesting dendrimer building blocks: A nonadiabatic perspective

J. Chem. Phys. (March 2024)

Dynamics of photoionization from molecular electronic wavepacket states in intense pulse laser fields: A nonadiabatic electron wavepacket study

J. Chem. Phys. (April 2017)

Simulating conical intersection dynamics in the condensed phase with hybrid quantum master equations

J. Chem. Phys. (July 2019)



The Journal of Chemical Physics

Special Topics Open for Submissions

[Learn More](#)

Wavepacket and reduced-density approaches for high-dimensional quantum dynamics: Application to the nonlinear spectroscopy of asymmetrical light-harvesting building blocks

Cite as: J. Chem. Phys. 162, 244102 (2025); doi: 10.1063/5.0270440

Submitted: 11 March 2025 • Accepted: 29 May 2025 •

Published Online: 23 June 2025



View Online



Export Citation



CrossMark

Joachim Galiana,^{1,a)}  Michèle Desouter-Lecomte,²  and Benjamin Lasorne^{1,b)} 

AFFILIATIONS

¹ ICGM, Univ Montpellier, CNRS, ENSCM, Montpellier, France

² Institut de Chimie Physique, Université Paris-Saclay-CNRS, UMR8000, F-91400 Orsay, France

^{a)} Current address: Departamento de Química, Universidad Autónoma de Madrid, Madrid, Spain.

^{b)} Author to whom correspondence should be addressed: benjamin.lasorne@umontpellier.fr

ABSTRACT

Excitation-energy transfer (EET) and relaxation in an optically excited building block of poly(phenylene ethynylene) (PPE) dendrimers are simulated using wavepackets with the multilayer multiconfiguration time-dependent Hartree (ML-MCTDH) method and reduced-density matrices with the hierarchical equations of motion (HEOM) approach. The dynamics of the ultrafast electronic funneling between the first two excited electronic states in the asymmetrically *meta*-substituted PPE oligomer with two rings on one branch and three rings on the other side, with a shared ring in between, is treated with 93-dimensional *ab initio* vibronic-coupling Hamiltonian (VCH) models, either linear or with bilinear and quadratic terms. The linear VCH model is also used to calibrate an open quantum system that falls in a computationally demanding non-perturbative non-Markovian regime. The linear-response absorption and emission spectra are simulated with both the ML-MCTDH and HEOM methods. The latter is further used to explore the nonlinear regime toward two-dimensional spectroscopy. We illustrate how a minimal VCH model with the two main active bright states and the impulsive-pulse limit in third-order response theory may provide at lower cost polarization-sensitive time-resolved signals that monitor the early EET dynamics. We also confirm the essential role played by the high-frequency acetylenic and quinoidal vibrational modes.

Published under an exclusive license by AIP Publishing. <https://doi.org/10.1063/5.0270440>

I. INTRODUCTION

The photophysics and ultrafast funneling dynamics in tree-like poly(phenylene ethynylene) (PPE) dendrimers have drawn great interest since their original synthesis in 1995.¹ They have been extensively studied, both experimentally^{2–6} and theoretically,^{7,8} for their astonishing light-harvesting properties. In the present work, we investigate such features in an asymmetrical building block of PPE dendrimers, for which we extract time-dependent spectral fingerprints of ultrafast electronic excitation-energy transfer (EET) from simulations with performant quantum-dynamics methods using an

ab initio calibrated vibronic coupling Hamiltonian (VCH) model in full dimensionality as regards in-plane motions.

In the present work, our system of interest for simulating such signals is the exhaustively studied asymmetrically *meta*-substituted PPE oligomer, made of four phenyl or phenylene rings and three acetylenic bonds, called m23 in the following [Fig. 1(a)]. This building block of PPE dendrimers was shown to be an ideal model system for EET, having two distinct localized excitons as its first two singlet electronic excited states [see Figs. 1(b) and 1(c)].^{9–11} Here, we use both wavepacket and reduced-density approaches to estimate electronic population dynamics, linear- and nonlinear

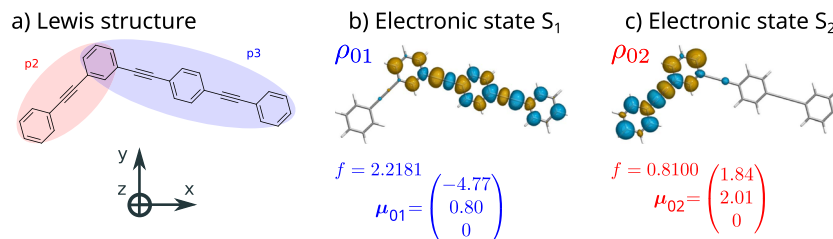


FIG. 1. (a) Lewis structure associated with the Franck–Condon geometry of the first asymmetrical *meta*-substituted PPE oligomer, called m23 in the following. The Cartesian axes are also given. (b) and (c) Transition density, oscillator strength, and transition dipole moment (in atomic units) for each of the first two singlet electronic excited states at the Franck–Condon geometry.

time-resolved spectroscopic signals, altogether to characterize ultrafast intramolecular EET in m23.

Alternative full-dimensional simulations of the photoinduced dynamics of m23 were originally exposed by Fernandez-Alberti and co-workers using the hybrid quantum–classical trajectory surface hopping (TSH) method^{9,12} and the multiconfiguration Ehrenfest approach.¹³ Such simulations have also been recently used to produce nonlinear spectroscopic signals to study exploitable spectral signatures of EET.^{14,15} The present work explores similar objectives but with completely different computational approaches.

We have recently proposed a quantum wavepacket study—based on the multiconfiguration time-dependent Hartree (MCTDH) method^{16,17}—of the photoinduced dynamics of m23 with dimensionally reduced VCH models obtained from its *ab initio* potential energy surfaces (PESs).¹¹ Such a strategy was concomitantly followed by other authors to go toward a higher-dimensional model, using a wavepacket tensor-train formalism.¹⁸ Here, we revisit the photodynamics of m23 with both the multilayer MCTDH (ML-MCTDH)^{19–21} wavepacket and the hierarchical equations of motion (HEOM)^{22–27} reduced-density approaches, using a systematic parameterization procedure for generating VCH models adapted to two-exciton systems in high dimensionality.

Wavepacket methods take their historical roots in simulating energy-resolved molecular photodissociation or light-absorption cross section spectra from time-dependent quantum dynamics, as triggered by the seminal work of Heller in the late 1970s that related the cross section spectrum to the Fourier transform of a wavepacket correlation function.²⁸ This is a linear-response approach based on first-order time-dependent perturbation theory.

More recently, some pressing questions have arisen within the theoretical/computational community about what we actually simulate and how we should better relate to time-resolved spectroscopy experiments beyond a linear response. Indeed, since Mukamel’s seminal studies,^{29,30} there has been a clear incentive for theoretical chemistry to address nonlinear and/or two-dimensional (2D) spectroscopy techniques, which are no longer exotic but rather the new standard.^{31–36} In particular, in the cases of photoinduced (energy or charge) transfers and chemical reactions, the relation between electronic populations and experimental observables has become central.

In addition, taking into account the role of the environment that surrounds the molecule (dissipation, solvent and thermal effects, etc.) with the reduced-density operator formalism has

become crucial again in this context. This has led to many flavors of open quantum dynamics approaches, one of them—used in the present work—being known as the HEOM method, in which vibrations are considered as a continuous bath (with a statistical spectral density) coupled to the discrete electronic subsystem (quantum few-level reduced-density matrix). We illustrate herein how a VCH model in a minimal electronic basis set and HEOM simulations in the strong system–bath coupling regime with approximate spectral densities may provide relevant information on spectroscopic signals monitoring the early EET in the m23 system as a complement to alternative semiclassical simulations.^{14,15}

This paper is organized as follows. In Sec. II, we describe our procedure for the realistic parameterization of both the discrete and continuous high-dimensional models that are used for ML-MCTDH and HEOM dynamics, respectively, and recall the underlying formalism for calculating various spectroscopic responses from simulations. In Sec. III, we first provide and compare time-resolved electronic populations and steady-state spectra obtained with both approaches within a linear response. We continue with an exposition of nonlinear and 2D spectra; in particular, we discuss transient polarization-sensitive signals and show how they provide a fingerprint for EET. Concluding remarks and outlook are gathered in Sec. IV.

II. METHODS AND CONCEPTS

A. The models and their Hamiltonians

1. High-dimensional vibronic coupling Hamiltonians

Within an *ab initio* adiabatic description, the electronic system of the m23 molecule is reduced herein to its electronic ground state, S₀, and its first two bright singlet electronic excited states, S₁ and S₂, which are nonadiabatically coupled and have been described in detail in previous studies.^{9–11}

The minima of the S₀ (Franck–Condon point, FCP), S₁, and S₂ states, and their frequencies, as well as the minimum-energy conical intersection (MECI) between S₁ and S₂, and its branching-space vectors, have all been optimized and characterized previously with DFT and TD-DFT calculations (CAM-B3LYP/6-31+G* level of theory)¹¹ using the GAUSSIAN 16 (Revision A.03) quantum-chemistry software package.³⁷ In particular, it has been shown that S₁ is locally excited on the 3-ring branch p3 (at 3.88 eV), while S₂ is locally excited on the shorter 2-ring branch p2 (at 4.55 eV).

The corresponding transition densities are shown in Figs. 1(b) and 1(c), together with the electronic transition dipole moments and oscillator strengths. Let us insist that we focus here on the two locally excited (excitonic-like within this pseudo-dimer) bright states. Potential charge-transfer-like dark states are weakly coupled to the locally excited ones (low differential overlap of $n\pi^*/\pi\pi^*$ -type) and are expected not to affect the ultrafast dynamics of EET (see, for example, our previous investigation in Ref. 38).

In order to run our simulations, we have parameterized a diabatic high-dimensional VCH model for the ground state S_0 and the two coupled PESs of the singlet electronic excited states S_1 and S_2 of m23 with all the $N = 93$ in-plane (A') normal modes of vibration. Such a type of model refers to as a “diabatization by ansatz.” At the FCP, the two excited diabatic states that form the interacting basis set, D_1 and D_2 , coincide with the adiabatic ones, S_1 and S_2 , by construction. All the in-plane modes are involved *a priori* in both the intra-state energy and inter-state coupling gradients for the first two electronic excited states (of same symmetry A'). Such a selection includes in particular the dominant quinoidal and acetylenic modes, previously identified as being essential for EET in the PPE dendrimers,^{9,11,39–41} here augmented with extra low-frequency modes and C–H vibrations.

Note that out-of-plane modes are soft and anharmonic distortions. In addition, the bright-excited-state bonding pattern is cumulenenic (double–double–double) and much more rigid than the alternate single–triple–single bonding pattern so that the molecules that have absorbed light are likely to stay planar in the early dynamics after excitation. In this situation, all relevant gradients and branching-space vectors are A' (in-plane). Hence, the out-of-plane motions are expected to play a dynamical role over the timescale of the overall rotations (>1 ps) and thus be treated as essentially inducing statistical spectral broadening as regards the ultrafast vibronic dynamics of the ideal planar system involved in the EET process.

Our most sophisticated model Hamiltonian is in between the customary linear vibronic coupling (LVC) and the full quadratic vibronic coupling (QVC) models; namely, the off-diagonal bilinear terms are set to zero here, but diagonal quadratic and bilinear terms remain flexible (three approximate flavors of it will be discussed in what follows). The model Hamiltonian matrix (centered at the FCP geometry) thus reads

$$\begin{aligned} \mathbf{H}(\mathbf{Q}) = & \begin{pmatrix} 0 & 0 & 0 \\ 0 & E^{(1)} & 0 \\ 0 & 0 & E^{(2)} \end{pmatrix} + \left(\widehat{T}_{\text{nu}} + \sum_i \frac{1}{2} k_i^{(0)} Q_i^2 \right) \mathbb{1}_3 \\ & + \sum_i \begin{pmatrix} 0 & 0 & 0 \\ 0 & \kappa_i^{(1)} Q_i & 0 \\ 0 & 0 & \kappa_i^{(2)} Q_i \end{pmatrix} + \sum_i \begin{pmatrix} 0 & 0 & 0 \\ 0 & 0 & h_i' Q_i \\ 0 & h_i' Q_i & 0 \end{pmatrix} \\ & + \sum_i \sum_j \begin{pmatrix} 0 & 0 & 0 \\ 0 & \frac{1}{2} \gamma_{ij}^{(1)} Q_i Q_j & 0 \\ 0 & 0 & \frac{1}{2} \gamma_{ij}^{(2)} Q_i Q_j \end{pmatrix}, \quad (1) \end{aligned}$$

where \widehat{T}_{nu} is a typical one-state normal-mode nuclear kinetic-energy operator and the second matrix (proportional to the identity matrix) is the harmonic reference, parameterized at the minimum of the

electronic ground state (FCP) through the knowledge of the frequencies $\omega_i^{(0)^2} = k_i^{(0)}$ (assuming mass-weighted normal coordinates, Q_i).

The curvatures of the electronic excited states are allowed to be different together and with the electronic ground state (thus including Duschinsky effects) thanks to the diagonal quadratic terms $\gamma_{ii}^{(s)}$. In other words, we model the PESs with a Taylor expansion to the second order for the diabatic potential energies (diagonal) and to the first order for the inter-state coupling (off-diagonal).

In the following, we shall refer to Eq. (1) as the LVC+ γ model. From it, we define the pure LVC model, upon setting the last matrix to zero (quadratic corrections and bilinear mode mixings). The intermediate model with quadratic corrections obtained from the LVC+ γ model but restricted to $i = j$ for γ_{ij} will be called LVC+ γ_{ii} .

The LVC model will be used as the system–bath Hamiltonian associated with our open quantum system (see below). Within second quantization, it may be termed a Frenkel–Holstein excitonic Hamiltonian (in relation to the p2 and p3 locally excited states) coupled to a harmonic bosonic bath, or a spin-boson model as regards the two-level excited manifold at the FCP (D_1 and D_2).

a. Local fitting procedure via identification of energy derivatives. Herein, we give details about the parameterization of the model Hamiltonian defined in Eq. (1). It uses (i) the vertical transition energies, gradients, and Hessians at the FCP and (ii) the position (with respect to FCP) of the MECI, $\Delta\mathbf{Q}_X$, and the branching-space vectors, (\mathbf{g}, \mathbf{h}) , at this geometry.

The strategy for ensuring that the diabatic and adiabatic states coincide at both the FCP and MECI geometries is similar to the one used in a previous study on a dimensionally reduced model for m23.^{11,42} The orthogonal pair of branching-space vectors (\mathbf{g}, \mathbf{h}) is numerically obtained from the Hessian of the squared energy difference at the MECI and is rotated into a pair of new branching-space vectors $(\mathbf{g}', \mathbf{h}')$ such that

$$\mathbf{h}' \cdot \Delta\mathbf{Q}_X = 0, \quad (2)$$

where the \mathbf{h}' -vector components define the off-diagonal parameters in Eq. (1). With the 93 selected normal modes, the parameterized rotation angle is $\theta = 18.82^\circ$, which accounts for a moderate photochemical reaction-path curvature (second-order relaxation) from FCP to MECI.

We now focus on the parameters for the diabatic potential energies. The diabatic energies at the FCP geometry, $E^{(s)}(\mathbf{Q} = \mathbf{0})$, simply identify to the adiabatic vertical transition energies of S_1 and S_2 . Similarly, the diabatic gradients can be made identical to the adiabatic gradients of S_1 and S_2 within a Hellmann–Feynman spirit for a local crude-adiabatic representation.

The generation of the curvatures and bilinear cross terms for the excited diabatic states is more involved. The matrices $\boldsymbol{\gamma}^{(s)}$ (which account for intra-state mode mixing) cannot be directly identified with the vertical transition Hessians of the adiabatic states S_1 and S_2 . Indeed, because we defined an inter-state coupling gradient, \mathbf{h}' , the definition of the diabatic Hessians [sums of the ground-state Hessian \mathbf{K}_{S_0} and the $\boldsymbol{\gamma}^{(s)}$ matrices] must reflect the effect of the coupling when producing the adiabatic Hessians. To ensure this, we define the

diabatic Hessians as, according to a second-order Jahn–Teller-type formula,⁴³

$$\begin{aligned}\mathbf{K}_{S_0} + \boldsymbol{\gamma}^{(1)} &= \mathbf{K}_{D_1} = \mathbf{K}_{S_1} + 2 \frac{\mathbf{h}'\mathbf{h}'^T}{E_{S_2} - E_{S_1}}, \\ \mathbf{K}_{S_0} + \boldsymbol{\gamma}^{(2)} &= \mathbf{K}_{D_2} = \mathbf{K}_{S_2} - 2 \frac{\mathbf{h}'\mathbf{h}'^T}{E_{S_2} - E_{S_1}}.\end{aligned}\quad (3)$$

Such an effect is physically motivated but occurs here to have little consequences numerically, only because the FCP energy gap, $E_{S_2} - E_{S_1}$, is large enough (a more detailed analysis is provided in the [supplementary material](#), Sec. SI-I and Fig. SI-1).

Let us recall that we have restricted ourselves to the 93 in-plane normal modes of the m23 molecule herein. Overall, the most important values of the Hessians occur to be on-diagonal. In other words, the normal modes of S_0 almost form an orthonormal eigenbasis for the Hessians of the excited states (almost diagonal matrices). This means that there is little mode mixing, as proven by the small magnitude of the elements of the matrices $\boldsymbol{\gamma}^{(s)}$. They are also shown in the [supplementary material](#), Fig. SI-1. Such an analysis can be related to the evaluation of Duschinsky matrices, only with the fact that, here, the excited states are computed at the same geometry as the ground-state equilibrium geometry.

However, let us examine, for the mode-mixing matrices, $\boldsymbol{\gamma}^{(s)}$, some finer features as regards the frequencies of the normal modes. There are greater values (hence greater mode mixing) for the group of quinoidal and acetylenic modes (from 1600 to 2400 cm^{-1}), both among them and with the other modes. To some extent, this is also true for the triangular modes (from 1000 to 1600 cm^{-1}), with significant mode-mixing among them (see the [supplementary material](#), Fig. SI-1).

The previous analysis can serve two different (but not unrelated) purposes: (i) finding mode-combination strategies for optimally taking into account the correlation between the strongly mixing modes and (ii) establishing relevant system–bath partitions with respect to active modes (as regards spectroscopy and EET) and spectator modes. Such considerations are expected to help in forming a rationale for designing an optimal tree for ML-MCTDH simulations under high-rank-tensor compression approaches.

b. Validity and limitations of the local fitting procedure. The electronic energies at the minimum of S_0 (FCP) are set with no

ambiguity from the onset. Now, in order to evaluate the validity of our VCH approximate descriptions, we should compare the energies of the *ab initio* S_1 and S_2 adiabatic states at some critical points (obtained with routine optimization procedures) to the model eigenvalues. The electronic energies at the minima of S_1 and S_2 , and at the MECI are given in [Table I](#).

First, we can remark the excellent energy agreement as regards the S_1 minimum (Min S_1) obtained within our 93-dimensional LVC+ γ model and the true S_1 minimum of the *ab initio* PESs. However, the S_2 minimum (Min S_2) obtained within our 93-dimensional LVC+ γ model occurs to merge numerically with an S_1/S_2 conical intersection, which is a perfectly acceptable situation when the MECI is peaked (the S_2 minimum is the MECI). Since the *ab initio* S_2 minimum (Min S_2) exists, the *ab initio* MECI should, in fact, be slopped (at least slightly). Such small discrepancies are to be expected from a model that is imperfect as regards anharmonicity effects. Yet, we expect that the semi-quantitative orders of magnitude shown here are good enough for our model to be relevant.

2. Parameterization as an open quantum system

An open quantum system results from the bipartite partition of a complex system into an active sub-system treated by quantum mechanics coupled to an environment described by collective bath modes and statistical mechanics.^{44–46} The corresponding generic Hamiltonian matrix of the full system is split into three contributions,

$$\mathbf{H} = \mathbf{H}_S + \mathbf{H}_{SB} + \mathbf{H}_B, \quad (4)$$

where \mathbf{H}_S is the Hamiltonian of the open biexcitonic (three-level) system, associated here with the partition of the electronic degrees of freedom from all the vibrational (bosonic) modes. It is represented by the first diagonal matrix of Eq. (1), with the energies at the FCP geometry of the ground state (set to zero) and of the two excited states, $E^{(1)}$ and $E^{(2)}$.

The environment is a collection of $N = 93$ harmonic vibrational modes centered at the origin (FCP point) and associated with the ground-state frequencies. It is represented by \mathbf{H}_B and given by the second matrix of Eq. (1).

Such bosonic modes are separated into N_{bath} baths that make the effective electronic energies and inter-state coupling fluctuate to

TABLE I. Energies in eV of the first two adiabatic and diabatic excited states at the critical points in the *ab initio* PESs (at the CAM-B3LYP/6-31+G* level of theory) and in the LVC model (8-dimensional, from previous work¹¹) and the LVC+ γ model (93-dimensional, from present work).

Model	Full-dimensional (<i>ab initio</i>) ^a			8-Dimensional (LVC)			93-Dimensional (LVC+ γ)		
Critical point	Min S_1	Min S_2	MECI	Min S_1	Min S_2	MECI	Min S_1	Min S_2	MECI ^b
$E(S_1)$	3.61	3.99	4.30	3.67	4.00	4.40	3.62	4.13	...
$E(S_2)$	4.62	4.17	4.30	4.59	4.23	4.40	4.64	4.13	...
$\Delta E(S_1-S_2)$	1.01	0.18	$<5 \times 10^{-4}$	1.08	0.23	$<5 \times 10^{-3}$	1.02	$<5 \times 10^{-3}$...
$E(D_1)$	3.67	4.01	4.40	3.64	4.13	...
$E(D_2)$	4.59	4.22	4.40	4.62	4.13	...

^aDiabatic energies are not determined directly from *ab initio* calculations but are post-processed for the VCH models.

^bFor the 93-dimensional VCH model, the effective MECI occurs to be peaked and thus merges with Min S_2 .

first order with respect to the \mathbf{H}_S reference. The system–bath coupling is given by the third and fourth matrices of the LVC model in Eq. (1). It can be recast as $\mathbf{H}_{SB} = \sum_n^{N_{\text{bath}}} \mathbf{S}_n B_n$, where \mathbf{S}_n are the matrices of the projection and transition operators with respect to the electronic states of the system. The corresponding excitonic Pauli-type system operators are $\hat{S}_1 = |1\rangle\langle 1|$, $\hat{S}_2 = |2\rangle\langle 2|$, and $\hat{S}_3 = |1\rangle\langle 2| + |2\rangle\langle 1|$.

The collective modes, B_n , are bosonic-type operators given here in a coordinate representation for notational simplicity. Note that they do not appear as such in the HEOM equations but only via their statistical correlation functions, as described below. Three collective modes B_n are used here ($N_{\text{bath}} = 3$). The first two, $B_1 = \sum_j \kappa_j^{(1)} Q_j$ and $B_2 = \sum_j \kappa_j^{(2)} Q_j$, are defined from the gradients of the PESs at the reference FCP geometry. They are called tuning collective modes since they make the electronic energy gap vary to first order. The third collective mode, $B_3 = \sum_j h_j' Q_j$, is the coupling mode, which induces a first-order electronic inter-state coupling.

The evolution of the system reduced-density matrix, $\rho_S(t) = \text{tr}_B[\rho(t)]$, obtained upon tracing out the bath degrees of freedom, is given by a non-Markovian master equation. When the bath is harmonic, it follows Gaussian statistics and the main tool of the master equation is the matrix of the two-time correlation functions of the bath collective modes, $C_{nn'}(t) = \langle B_n(t) B_{n'}(0) \rangle_{\text{eq}}$, where $B_n(t)$ is the time-evolved Heisenberg representation of the operator and $\langle \bullet \rangle_{\text{eq}}$ denotes the average over a Boltzmann distribution at some given temperature T . We neglect here any correlation among the modes of the three baths and consider only diagonal terms $C_{nn}(t) = \langle B_n(t) B_n(0) \rangle_{\text{eq}}$, with $n = 1, 2, 3$, which will further be denoted $C_n(t)$ with a single index for the sake of simplicity. The correlation functions may be computed with molecular dynamics in order to have an exhaustive description of the solvent.^{47–49} In this work, it is obtained via the spectral densities that encode the interaction of the baths at each frequency.

In a first step, discrete spectral densities involving the LVC Hamiltonian parameters only are given by

$$J_n(\omega) = \frac{\pi}{2} \sum_k \frac{f_j^{(n)2}}{\omega_j} \delta(\omega - \omega_j), \quad (5)$$

where $f_j^{(n)} = \kappa_j^{(n)}$ for the tuning baths, $n = 1, 2$, and $f_j^{(3)} = h_j'$ for the coupling bath. They peak at all individual vibrational frequencies, ω_j , and form a Dirac comb. In order to account qualitatively for the existence of some dissipative environment and decaying mechanisms, the Dirac delta distributions are broadened by a single spectral width, Γ , so as to be approximated as Lorentzian functions,

$$\delta(\omega - \omega_j) \sim \frac{1}{\pi} \frac{\Gamma}{(\omega - \omega_j)^2 + \Gamma^2}, \quad (6)$$

thus leading to a continuous spectral density. This is a typical smoothing approach that has been used in another context (MCTDH dynamics) in order to systematically reduce the number of active modes.^{50,51} In the absence of any further information on the dissipative environment, we adopted this heuristic procedure and took $\Gamma = 80 \text{ cm}^{-1}$, giving a spectral line enlargement of the same order of magnitude as in a previous simulation on the m22 dimer.⁴¹ The corresponding spectral densities are shown in Fig. 2.

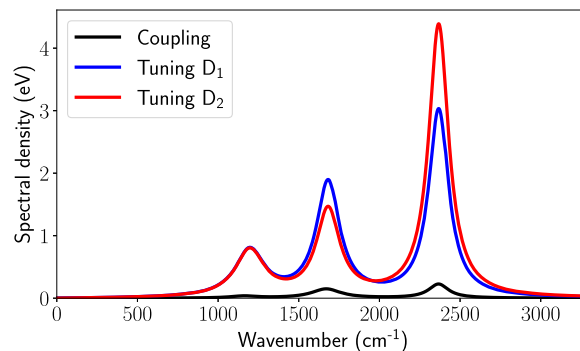


FIG. 2. Spectral densities associated with the correlation functions for the three baths (tuning for D_1 , tuning for D_2 , and inter-state coupling between them).

Within this context, the correlation functions are given by the following Fourier transforms:

$$C_n(t - t') = \frac{\hbar}{\pi} \int_{-\infty}^{\infty} d\omega J_n(\omega) \tilde{n}_\beta(\omega) e^{-i\omega(t-t')}, \quad (7)$$

where $\tilde{n}_\beta(\omega) = (1 + \coth(\beta\hbar\omega/2))/2$ is the temperature-dependent Bose function with $\beta = 1/k_B T$, in which k_B is the Boltzmann constant. We take here the standard room temperature, $T = 298 \text{ K}$. In addition, let us stress out here that the symbol ω , as used in our various equations, duly refers to an actual angular frequency (an angle variation per unit of time). However, for the sake of ease of comparison, we customarily provides its values in terms of its equivalent wavenumber (given in reciprocal centimeters), such as in Fig. 2.

B. Propagated quantities and time-evolution equations

1. Quantum wavepacket propagation

Using the aforementioned VCH models, quantum dynamics calculations were carried out using the ML-MCTDH method, as first implemented in the Heidelberg MCTDH package and further integrated to the QUANTICS suite of quantum-dynamics programs.^{16,17,52}

The ML-MCTDH wavefunction was defined by building a simple tree reflecting the different types of molecular vibrations among the 93 in-plane normal modes. The separation of the branches in the first layer of the tree is based on the frequencies and reduced masses of the normal modes, sorted into four groups defined in the [supplementary material](#). The latter group also reflects the three-peak features of the spectral density shown in Fig. 2. The rest of the three was built in a simple iterative manner down to the last layer where the individual modes are combined two by two.

The number of single-particle functions (SPFs) for each node and combined modes was chosen so as to maintain a reasonable computational time (<24 h of human time on a 16-core CPU for 200 fs) and small lowest natural weights ($<1 \times 10^{-2}$) throughout the simulation. A detailed representation of the ML-tree is given in the [supplementary material](#), Fig. SI-3.

2. Hierarchical equations of motion

The HEOM method^{22–26,53} for simulating the dissipative dynamics of an open quantum system relies on solving a non-Markovian master equation. It is exact for harmonic baths characterized by Gaussian statistics when the hierarchy is truncated soundly. The central point of the HEOM formalism is the expansion of the correlation functions for each bath, $C_n(t)$, and of their complex conjugates, $\bar{C}_n(t)$, as sums of ordered contributions. The most popular expression, adopted here, is a weighted sum of K_n rotating and decaying exponential functions,

$$C_n(t) = \sum_{k=1}^{K_n} \alpha_k^{(n)} e^{i\gamma_k^{(n)} t}, \quad (8)$$

with complex amplitudes α_k and phases $\gamma_k = \Omega_k + i\Gamma_k$. Every term corresponds to a so-called bath artificial decay mode, with a positive decay rate, Γ_k , and a positive or negative rotating frequency, Ω_k , associated with the absorption or emission energy between the system and the bath. The Fourier transform [Eq. (7)] provides analytical expressions of the α_k , $\bar{\alpha}_k$, and γ_k coefficients^{54,55} when the spectral density is fitted by a sum of Tannor–Meier Lorentzian functions,⁵⁶

$$J(\omega) = \sum_{l=1}^{n_{\text{lor}}} \frac{p_l \omega}{\hbar^3 [(\omega + \Omega_l)^2 + \Gamma_l^2] [(\omega - \Omega_l)^2 + \Gamma_l^2]}. \quad (9)$$

The expressions of the α_k and γ_k parameters related to this Tannor–Meier method are summarized in the [supplementary material](#), Sec. SI-V.A. For each bath, the spectral density was fitted here in practice by a sum of three functions, $n_{\text{lor}} = 3$. The values of the parameters of the Lorentzian functions are given in the [supplementary material](#), Table SI-I.

The HEOM formalism consists in a local-in-time system of coupled equations among auxiliary matrices, also called auxiliary density operators (ADOs) having the dimension of the system reduced-density matrix, here 3×3 . The coupled equations involve only the parameters of the correlation function [Eq. (8)] and the system–bath operators. They are summarized in the [supplementary material](#), Sec. SI-V.A. At room temperature, we neglect the poles coming from the Bose function [Eq. (7)] called the Matsubara frequencies. This approximation notably reduces the computational effort and, nevertheless, allows a satisfactory qualitative description. However, their consideration is crucial at very low temperatures where their number becomes very large and requires different strategies to overcome the computational difficulties due to the prohibitive number of ADOs.^{55,57} Note that the fit by only some Tannor–Meier Lorentzian functions smooths out some structures and provides an average description. Different HEOM strategies could be used, such as the free-pole method⁵⁷ or the discretization of the spectral density with undamped modes.⁵⁸ We have compared different approaches in a previous paper for a similar system (the symmetrical dimer parent, m22) involving only two baths.⁵⁵ However, in the present case of m23, we use three baths and the computational cost should become prohibitive with a standard implementation of HEOM. This is illustrated with the increase in the number of matrices with the number of modes in the [supplementary material](#) (SI-Table II).

The HEOM coupled equations were solved according to standard encoding within the adaptive Runge–Kutta method or within a tensor-train format, as described in Refs. 53 and 55.

C. Simulation of spectroscopic signals

We first present here the typical approaches based on linear-response theory to obtain the steady-state absorption and emission spectra, using the ML-MCTDH or HEOM formalisms. Then, we summarize the main relations derived from the third-order optical response functions to simulate time-dependent spectroscopy with HEOM.^{23,24,59–65}

1. Steady-state absorption and emission spectroscopy

The linear-response steady-state absorption and emission spectra obtained with quantum wavepacket dynamics, here within the ML-MCTDH formalism, are typically computed as the power spectra of autocorrelation functions.

Let us define without loss of generality a molecular wavepacket within a (1+2)-manifold of diabatic electronic states (the ground state and two excited states) as a set of three components,

$$\Psi(\mathbf{Q}, t) = (\psi_0(\mathbf{Q}, t) \quad \psi_1(\mathbf{Q}, t) \quad \psi_2(\mathbf{Q}, t))^T. \quad (10)$$

For a given initial state, $\Psi(t=0)$, we define the autocorrelation function as

$$c(t) = \langle \Psi(0) | \Psi(t) \rangle, \quad (11)$$

where integration is performed over the nuclear degrees of freedom, \mathbf{Q} , according to standard Dirac's bra–ket notations.

Unless otherwise specified, the so-called $t/2$ -trick can be used (always valid for a real-valued initial wavepacket and a Hermitian Hamiltonian, according to time-reversibility and unitary propagation),

$$c(t) = \langle \Psi(-t/2) | \Psi(t/2) \rangle. \quad (12)$$

From an infinite propagation time, we should obtain the power spectrum associated with the propagation of this initial wavepacket upon taking the Fourier transform of the autocorrelation function,

$$\sigma(\omega) \propto \int_{-\infty}^{\infty} c(t) e^{i\omega t} dt. \quad (13)$$

Because, numerically speaking, the final propagation time, t_f , is always finite, the autocorrelation function has to be multiplied by some periodic and smoothly decaying function, for example $g(t) = \cos^n(\pi t/2t_f)$, in order to make the Fourier-transformed signal well-behaved and avoid the so-called Gibbs phenomenon over the finite time window ($n = 1$ in this work). An extra artificial dissipative broadening was also applied upon convoluting the spectra with a Lorentzian, hence multiplying the autocorrelation function with a damping function $\exp(-t/\tau)$, with an *ad hoc* damping time $\tau = 60$ fs corresponding to a half-width at half-maximum (HWHM) of 88 cm^{-1} , so as to mimic the numerical spectral widths effectively obtained from HEOM linear-response simulations of the same spectra (related to, but not to be confused with the Lorentzian HWHM parameter, $\Gamma = 80 \text{ cm}^{-1}$).

Such a time-to-energy procedure largely depends on how we define the initial state. For the absorption spectrum, we typically

assume a sudden excitation of the ground-state vibrational wavefunction from the electronic ground state to each of the two electronic excited states. For the emission spectrum, the relaxed vibronic eigenstate within the excited state manifold must be computed beforehand. In a strongly coupled and high-symmetrical situation such as in our previous work on the m22 dimer,⁴¹ we could have considered each component of the superposition of the two vibrational contributions for each diabatic state and perhaps play with various mixtures. However, for m23, the electronic population ratio in the relaxed vibronic state is so close to one in the lowest diabatic state that we considered as a good approximation that we could reduce it to its single component in $D_1 \approx S_1$.

The customary state-to-state power spectra given in Eq. (13) are independent of the transition dipole moments. They can be further summed with relative weights that reflect both transition dipole strengths so as to produce a total spectrum. This is here one of the main differences in computing linear spectra for the two approaches (wavepackets or reduced-density matrices), which is related to the way that the excitation is modeled. Within the HEOM description, the polarization of the electric field is included from the onset so that all the electronic excited states having nonzero transition dipole moments are absorbing. Within the (ML-)MCTDH description, the polarization is not directly taken into account, and one has to decide from the onset which of the two electronic excited states is absorbing.

While such simulations based on wavepacket quantum dynamics and Fourier transforms are now routinely used for the simulation of steady-state spectroscopy, their extensions to nonlinear spectroscopies—requiring a third response formalism as in here—are becoming pressing matters. For instance, a recent and striking example of such an application based on the MCTDH formalism can be found in Ref. 35.

Now, as regards HEOM, the absorption and emission spectra within a linear response are written as follows (involving an ultimate over-the-system trace):

$$\sigma^{\text{abs}}(\omega) = \text{Re}\left\{\text{FT}\left[\text{tr}_S\left(\rho_{\mu_+}^\dagger(t)\rho_{\mu_+}(0)\right)\right]\right\}, \quad (14)$$

$$\sigma^{\text{em}}(\omega) = \text{Re}\left\{\text{FT}\left[\text{tr}_S\left(\rho_{\mu_-}^\dagger(t)\rho_{\mu_-}(\text{eq})\right)\right]\right\}, \quad (15)$$

where the prefactor proportional to ω or ω^3 for absorption and emission, respectively, has been set equal to one for simplicity and FT designates the Fourier transform.

The density matrices involved in them are built from the excitonic lowering and raising (transition-dipole) operators,

$$\mu_-^{(p)} = \sum_{j=1}^2 \mu_{0j,p}|0\rangle\langle j| \quad (16)$$

and

$$\mu_+^{(p)} = \sum_{j=1}^2 \mu_{0j,p}|j\rangle\langle 0|, \quad (17)$$

where $p = x$ and $p = y$ denote the electric-field polarization directions along the x - and y -axes, respectively, within the molecular plane (see Fig. 1).

For the absorption, $\rho_{\mu_+}(0) = \sum_p \mu_+^{(p)} \rho_S(0)$ and all the ADOs are set to zero initially. For the emission, the lowering operator acts

on the system density matrix $\rho_{\mu_-}(\text{eq}) = \sum_p \mu_-^{(p)} \rho_S(\text{eq})$ and on all the ADOs obtained when the equilibrium vibronic state within the excited electronic manifold—denoted eq—has been reached after relaxation. We consider different possibilities for the polarization: either parallel to the unit vectors e_x or e_y (see Fig. 1), or also (for completion, since the definition of the two axes is quite arbitrary), along another oblique direction, along the unit vector $(e_x + e_y)/\sqrt{2}$. The first two cases will be referred to as XX and YY and lead to an initial condition with a superposed electronic state, $\mu_{01,x}|D_1\rangle + \mu_{02,x}|D_2\rangle$ or $\mu_{01,y}|D_1\rangle + \mu_{02,y}|D_2\rangle$. The oblique polarization, further denoted $(X + Y)(X + Y)$, corresponds to the preparation of the superposed state $(\mu_{01,x} + \mu_{01,y})|D_1\rangle + (\mu_{02,x} + \mu_{02,y})|D_2\rangle$ (up to renormalization).

2. Nonlinear spectroscopy

We now expose the formal ingredients for the simulation of time-frequency resolved or two-dimensional (2D) spectra (in particular within the HEOM formalism) when assuming delta-like pump-probe laser pulses. In particular, we show how this impulsive approximation allows us to simulate significant polarization-dependent spectroscopic signals that provide fingerprints of the EET. We first recall the general formalism of multi-time correlation functions, which are involved in nonlinear 2D spectroscopy.³⁰

The third-order optical response function $R^{(3)}(t_3, t_2, t_1)$ that describes the system response to the light-induced perturbations is abundantly documented.^{29–31,33–36,66–70} The simulation of the 2D photon echo spectra involves the interaction between the system and three laser pulses at times τ_1 , τ_2 , and τ_3 separated by delay times t_1 and t_2 , generating a third-order polarization after a time interval t_3 as schematized in Fig. 3.

The first pulse prepares an optical coherence between the excited states and the ground state so that the field-free evolution during t_1 is customarily called the coherence time. The second pulse creates a population in the excited manifold or in the ground state, and the next free evolution time t_2 is the waiting or population time. The third pulse probes the system after this delay t_2 before detection after the t_3 time interval. The third-order polarization is then obtained by convolution with the laser pulses centered at τ_1 , τ_2 , and τ_3 , respectively (see Fig. 3). They are each characterized by their

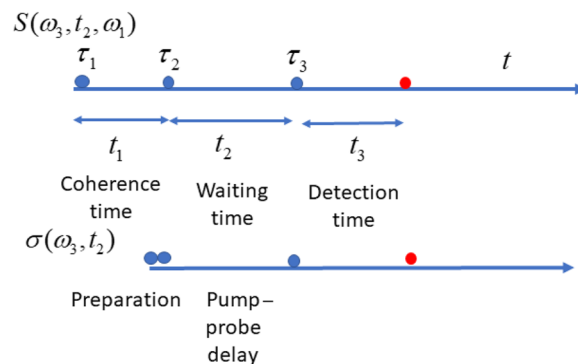


FIG. 3. Scheme of the principle of the three time intervals involved in the computation of 2D photon echo spectra involving Fourier transforms with respect to t_1 and t_3 or of the ESE [Eq. (23)], GSB [Eq. (24)], or TA [Eq. (22)] spectra, for which $t_1 = 0$ and the Fourier transform is over t_3 .

polarization, wave vector k , frequency, envelope, and initial phase. Spectra derived from the third-order response $R^{(3)}(t_3, t_2, t_1)$ without convolution with laser pulses are thus ideal spectra that would involve interactions with pulses described by delta distributions $\delta(t)$.

The response function

$$R^{(3)}(t_3, t_2, t_1) = R_{\text{rp}}(t_3, t_2, t_1) + R_{\text{nr}}(t_3, t_2, t_1) \quad (18)$$

may be split into two contributions, the rephasing one, R_{rp} (with detected wave vector $k = -k_1 + k_2 + k_3$), and the non-rephasing one, R_{nr} (with $k = k_1 - k_2 + k_3$). The 2D spectrum for a given waiting time t_2 is obtained by two Fourier transforms,

$$S(\omega_3, t_2, \omega_1) = \text{Re} \int_0^\infty dt_1 \int_0^\infty dt_3 e^{i\omega_1 t_1 + i\omega_3 t_3} R_{\text{nr}}(t_3, t_2, t_1) + \text{Re} \int_0^\infty dt_1 \int_0^\infty dt_3 e^{-i\omega_1 t_1 + i\omega_3 t_3} R_{\text{rp}}(t_3, t_2, t_1). \quad (19)$$

The integral over the ω_1 frequency,

$$\sigma(\omega_3, t_2) = \int_0^\infty S(\omega_3, t_2, \omega_1) d\omega_1, \quad (20)$$

is the transient absorption (TA). Within the field of time-resolved spectroscopy, TA is usually defined as the differential absorbance within a pump-probe context: namely, $\Delta A = A(\text{w/pump}) - A(\text{w/o pump})$ (aka. differential optical density). Hereby, we investigate TA from the three-pulse photon-echo 2D polarization upon assuming that the first two pulses overlap.^{30,70} TA bears some resemblance with the so-called transient grating (TG) signal because the third-order polarization in TA is identical to that in TG; only the measurements are different in TA and TG.⁷¹ The time t_2 takes the meaning of a delay between the pump and a probe. For the sake of convenience, the subscripts are removed for t_2 and ω_3 and the time-dependent spectrum in Eq. (21) is denoted $\sigma^{\text{TA}}(\omega, t)$. Note that specific polarizations may be used for the pump and the probe for polarization sensitive signals. They will be specified when necessary. By using Eq. (19) with overlapping first two pulses, the computation of $\sigma^{\text{TA}}(\omega, t)$ involves the responses for $t_1 = 0$,

$$\sigma^{\text{TA}}(\omega, t) = \text{Re} \int_0^\infty dt_3 [R_{\text{nr}}(t_3, t, 0) + R_{\text{rp}}(t_3, t, 0)] e^{i\omega t_3}. \quad (21)$$

The expressions of the responses for HEOM simulations are detailed in the [supplementary material](#), Sec. SI-VI.A. In principle, $\sigma^{\text{TA}}(\omega, t)$ is the sum of three contributions related to different absorption or emission processes: $\sigma^{\text{ESE}}(\omega, t)$ describes the excited-state stimulated emission (ESE), $\sigma^{\text{GSB}}(\omega, t)$ corresponds to the ground-state bleaching (GSB), and $\sigma^{\text{ESA}}(\omega, t)$ gives the excited-state absorption (ESA). The ESA process is not considered here because the electronic basis set is truncated to the ground and the two D_1 and D_2 excited states. In our simulations, we consider

$$\sigma^{\text{TA}}(\omega, t) = \sigma^{\text{ESE}}(\omega, t) + \sigma^{\text{GSB}}(\omega, t). \quad (22)$$

We refer to the [supplementary material](#), Sec. SI-VI.A, for more details, and we give here only the final operational expressions for the specific response functions involved in ESE and GSB. We have

$$\sigma^{\text{ESE}}(\omega, t) = \text{Re} \int_0^\infty dt_3 e^{i\omega t_3} R^{\text{ESE}}(t_3, t, 0) \quad (23)$$

and

$$\sigma^{\text{GSB}}(\omega, t) = \text{Re} \int_0^\infty dt_3 e^{i\omega t_3} R^{\text{GSB}}(t_3, t, 0), \quad (24)$$

with

$$R^{\text{ESE}}(t_3, t_2, t_1) = \langle \tilde{\mu}_- G(t_3) \{ G(t_2) [G(t_1) (\tilde{\mu}_+ \tilde{\rho}_0) \tilde{\mu}_-] \tilde{\mu}_+ \} \rangle \quad (25)$$

and

$$R^{\text{GSB}}(t_3, t_2, t_1) = \langle \tilde{\mu}_- G(t_3) \{ \tilde{\mu}_+ G(t_2) [G(t_1) (\tilde{\rho}_0 \tilde{\mu}_-) \tilde{\mu}_+] \} \rangle. \quad (26)$$

There, $\tilde{\rho}_0$ represents a vector of matrices formed by the system density matrix and all the ADOs. At the initial time, all the ADOs are nil and the system is in the ground electronic state. $G(t)$ is the HEOM propagator driving the ensemble of HEOM matrices during a time t_1 , t_2 , or t_3 . $\tilde{\mu} = I_N \otimes \mu$, where I is the identity matrix, N is the number of HEOM matrices, and μ is the dipole transition matrix of the system. This means that this μ matrix must be applied to the system density matrix and to every ADO.²³ The relevant polarization must be specified for each application of the lowering or raising transition operators. The notation $\langle \bullet \rangle$ means here the final trace over the system. The trace over the bath is implicitly done by the HEOM propagator. The order of the right or left applications of the transition matrix after the propagation during the specific time intervals are explained in the [supplementary material](#), Sec. SI-IV.A. When $t_1 = 0$, one has $G(t_1 = 0) = 1$, and the right part of the bracket describes the initial state that is assumed to be prepared by an impulsive delta-like pulse. For ESE, this initial state, $\mu_+ \rho_0 \mu_-$, is the system reduced-density matrix of a superposition of the excited states weighted by the transition dipoles. For GSB, from Eq. (26), the initial state is the ground state populated with the norm of the previous superposition. However, each initial state can be renormalized for convenience.

The GSB contribution does not depend on t_2 in the particular case of the time-dependent transient absorption spectra when computed by using the response for $t_1 = 0$, making a grid only along t_2 and t_3 and assuming impulsive laser pulses. Such a situation is discussed in the authoritative book by Mukamel (Chap. 11).³⁰ In the HEOM case, the system is in the ground state and the bath is at equilibrium (with nil ADOS). Whatever the value of t_2 , the total system remains the same as before the excitation and the following correlation function does not change. Within a wavepacket approach, the system is either described by an eigenstate or by a Boltzmann mixture of eigenstates, and only a phase is varying with t_2 without any effect on the spectrum, as expected. Note that, for our 2D-spectroscopy simulations, the responses (rephasing and non-rephasing) are computed for grids along t_1 and t_3 and the GSB is not taken as a constant. Thus, σ^{GSB} corresponds to the absorption spectrum of the linear response up to an arbitrary factor, which disappears when normalizing. Similarly, the ESE contribution evolves toward the stationary emission spectrum of the linear response when the delay t (t_2) becomes sufficiently long. Using the $R^{\text{ESE}}(t_3, t, 0)$ response involves a specific initial superposed state, but the new equilibrated thermal state for long t_2 is, in principle, independent of the initial state. Both the absorption and emission spectra of the linear response are limiting cases of the time-dependent approach.

Integrated signals over the ω (ω_3) frequency contain quite significant fingerprints of the dynamics within the excited manifold. In

addition, they are easy to compute via the response functions since one has

$$S^{\text{TA}}(t) = \int_0^\infty d\omega (\sigma^{\text{ESE}}(\omega, t) + \sigma^{\text{GSB}}(\omega, t)) = S^{\text{ESE}}(t) + S^{\text{GSB}}(t) \\ = R^{\text{ESE}}(0, t, 0) + R^{\text{GSB}}(0, t, 0). \quad (27)$$

$S^{\text{ESE}}(t)$ gives the surface area of the emission spectrum. As $R^{\text{GSB}}(0, t, 0)$ does not depend on the delay t , it is just a constant and $S^{\text{ESE}}(t)$ is the main component. When the main active excited states are populated by different transition dipole components, polarization-sensitive detection of these integrated signals may provide different types of information about the energy transfer. As illustrated below, the diagonal cases, $S_{\text{XX}}^{\text{TA}}(t)$ or $S_{\text{YY}}^{\text{TA}}(t)$, are linked to the decay of the electronic coherence in a purely dephasing case or of the population or both. An off-diagonal case, $S_{\text{YX}}^{\text{TA}}(t)$ or $S_{\text{XY}}^{\text{TA}}(t)$, probes the increase in population in the final state. Finally, by combining detection signals with parallel or perpendicular polarizations, one gets insights into the rotation of the polarization by the anisotropy decay signal,

$$r(t) = \frac{S_{\parallel}^{\text{TA}}(t) - S_{\perp}^{\text{TA}}(t)}{\Delta S_{\text{iso}}(t)}, \quad (28)$$

where $\Delta S_{\text{iso}}(t)$ is the isotropic absorption difference,

$$\Delta S_{\text{iso}}(t) = S_{\parallel}^{\text{TA}}(t) + 2S_{\perp}^{\text{TA}}(t). \quad (29)$$

Such a polarization-sensitive analysis has been proposed in the literature to decipher the different electronic or vibrational coherences during the relaxation.^{64,72}

III. RESULTS AND DISCUSSION

We present herein population dynamics and spectroscopic linear and non-linear signals revealing EET with ML-MCTDH simulations using the full vibronic model and with HEOM using spectral densities parameterized by the Tannor–Meier method. For the particular system investigated here, the computational effort happens

to increase quite heavily as regards the convergence threshold, especially when generating multidimensional time grids for non-linear spectroscopy. Our strategy here is to consider decent enough models for ensuring relevant semi-quantitative results at reasonable computational time. The first approximation concerns the spectral density. When the full density is retained with the three peaks for each bath, the model is denoted “3L model” for three Lorentzian functions per bath. It is expected that the most important modes are those at high frequencies corresponding to the acetylenic vibrations and to the quinoidal distortions. By cutting off the low frequency peak in each bath, we define the “2L model” focusing on the two peaks around 1600 and 2300 cm^{-1} . The second approximation is relative to the HEOM level. The convergence tests are presented in the [supplementary material](#), Secs. SI-V.C and SI-V.I.E. We further discuss there the computational effort related to the increase in the number of matrices with the level and with Matsubara terms. We also illustrate that using a near-converged level may, nevertheless, provide relevant semi-quantitative information. Such a strategy appears as being a good balance for exploring such a complex system with three baths that are strongly coupled to the electronic system.

A. EET dynamics

We first probe the characteristics of intramolecular EET within the m23 molecule by applying a sudden excitation from the ground state to the second electronic excited state. In practice, this is achieved upon initializing the system with the ground-state equilibrium wavepacket or reduced-density and placing it at $t = 0$ in the diabatic state localized on the p2 branch (D_2 , so-called donor state). From this initial state, the system is propagated within the excited-state manifold, allowing transfer to the diabatic state localized on the p3 branch (D_1 , so-called acceptor state). The electronic population transfer is shown in [Fig. 4](#) (left panel) for both ML-MCTDH and HEOM dynamics for the full 3L model. A comparison with the 2L model is given in the [supplementary material](#), Figs. SI-8 and SI-10.

Population inversion occurs after around 20 fs in all types of simulations. Comparing the time evolution in the case of the LVC model only, we see that the population transfer calculated within

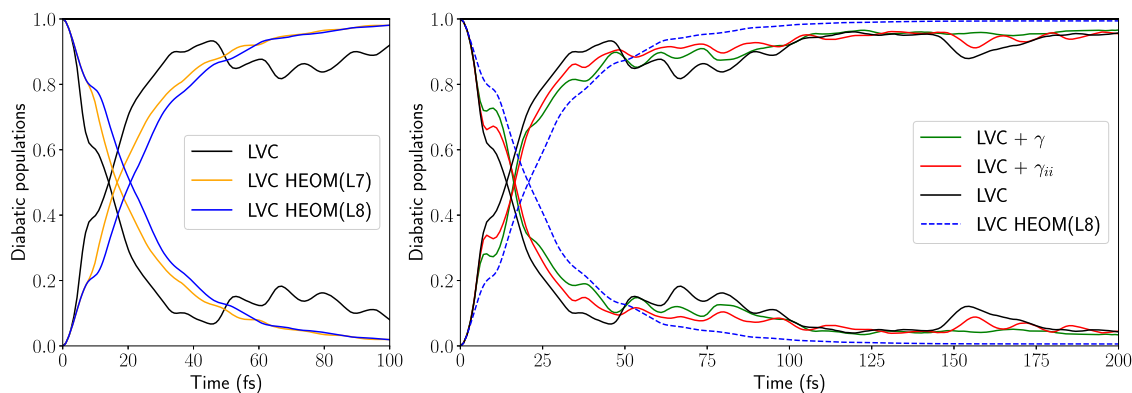


FIG. 4. Diabatic populations for different models and propagation methods for the simulation of EET. Left: comparison of the use of the ML-MCTDH and HEOM (hierarchy levels L7 and L8) formalisms with the LVC model. Right: comparison of the use of the LVC, $\text{LVC} + \gamma_{ii}$, and $\text{LVC} + \gamma$ models within the ML-MCTDH formalism, up to longer timescales.

the HEOM formalism is slightly slower than the one computed with a discrete definition of the modes (ML-MCTDH). Note that it is not surprising to keep observing sustained oscillations in populations calculated with a wavepacket method, since we are really simulating a finite, isolated, and closed system microcanonically (the broadening is phenomenological and only introduced after, at the Fourier-transform stage, to get a spectrum with realistic peak widths), while HEOM is a dissipative and canonical method per construction and is expected to provide full monotonic decay eventually. We also note that the more advanced case with eight hierarchy levels (L8) yields slightly delayed transfer dynamics compared to L7. This seems to be correlated with accounting for the small time lag due to the inflection feature around 10 fs, also observed in ML-MCTDH results.

The ML-MCTDH propagation has also been carried out with the more advanced LVC+ γ_{ii} and LVC+ γ models, which include second-order “intra-state couplings.” The results are shown in Fig. 4 (right panel) for longer timescales (up to 200 fs). The three models with the same propagation method (ML-MCTDH and similar ML-tree) exhibit small differences. The LVC model yields faster population transfer than the models including different curvatures (quadratic intra-state couplings) and mode mixing (bilinear intra-state couplings). This, again, goes with a smaller time lag associated with a less pronounced inflection feature around 10 fs. After population inversion, the LVC model exhibits less stability once the acceptor state is populated (see around 75 fs and 150 fs for instance). The more we account for intra-state couplings (quadratic, LVC+ γ_{ii} , and all bilinear, LVC+ γ), the more monotonic are the transfer to and the relaxation in the acceptor state.

The mode-mixing parameters slow down the population transfer dynamics but are eventually required to better relax toward the equilibrium geometry of the diabatic potential energy surfaces. This is consistent with a slightly stronger damping of the oscillatory features in the diabatic coherence, as shown in Fig. 5. This means that the mode-mixing parameters somewhat enhance “internal dissipation” for the ML-MCTDH calculations, which is included from the onset in an *ad hoc* manner within the HEOM approach.

Again, we stress here that our estimation of the mode-mixing parameters is done thanks to the energy derivatives with respect

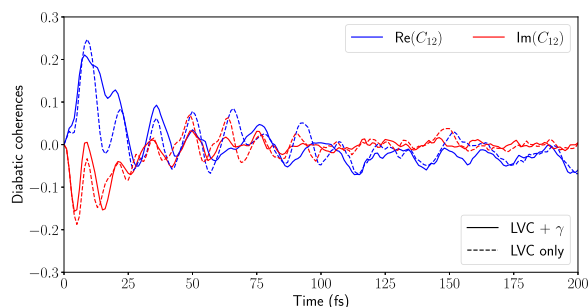


FIG. 5. Real and imaginary parts (blue and red lines, respectively) of the diabatic coherence for the LVC+ γ and LVC only models, with solid and dashed lines, respectively.

to a large number of degrees of freedom. A more involved discussion of the importance of mode-mixing parameters, in particular as regards reducing dimensionality, is made in the [supplementary material](#), Sec. SI-I.

B. Steady-state spectroscopy

For ML-MCTDH, the exact same methodology as in a previous study for a reduced model is used to compute power spectra within the realm of steady-state (or linear) spectroscopy.¹¹ Two contributions, $\sigma^{(1)}(\omega)$ and $\sigma^{(2)}(\omega)$, are computed for the absorption spectrum (toward the D₁ and D₂ states, respectively) and one for the emission spectrum toward the ground state. In addition, we estimate the total absorption spectrum as

$$\sigma^{\text{Total}}(\omega) = (\mu_{01,x}^2 + \mu_{01,y}^2)\sigma^{(1)}(\omega) + (\mu_{02,x}^2 + \mu_{02,y}^2)\sigma^{(2)}(\omega), \quad (30)$$

which is further normalized. The weighting is isotropic as regards the polarization direction. It is also consistent with a sudden approximation for the excitation of both electronic excited states with electronic transition dipole strengths at the Franck–Condon point as effective weights for each contribution. They are all shown in Fig. 6 (left panel) for the LVC+ γ model.

Note that the emission spectrum is approximated as the power spectrum initialized with the most important vibrational contribution in the ground vibronic eigenstate of the excited state manifold (with more than 99% population in the D₁ electronic state) and projected to the electronic ground state.

The same is done in Fig. 6 (center panel), obtained with the LVC model in order to compare with the HEOM linear-response spectrum obtained for the 3L model with the approximate level L7 without Matsubara terms. The convergence tests and comparison with the 2L model are presented in the [supplementary material](#), Sec. SI-V.C. Let us recall that the total absorption spectrum to both excited states with HEOM is obtained *a posteriori* by summing the spectra of the XX and YY cases so as to reproduce the weighting given in Eq. (30). Both absorption and emission spectra compare well for the two methods. We observe a larger discrepancy in the spectral region after 4.0 eV, corresponding to the transitions toward the D₂ electronic excited state.

In Fig. 6 (right panel), we now compare the results obtained by applying some specific oblique polarization [case (X + Y)(X + Y)] for checking its effect,

$$\sigma^{\text{Oblique}}(\omega) = (\mu_{01,x} + \mu_{01,y})^2 \sigma^{(1)}(\omega) + (\mu_{02,x} + \mu_{02,y})^2 \sigma^{(2)}(\omega). \quad (31)$$

The oblique absorption spectrum, $\sigma^{\text{Oblique}}(\omega)$, is obtained with ML-MCTDH from the isolated spectra with weights in the sum that are different from the previous case, $\sigma^{\text{Total}}(\omega)$. With HEOM, the oblique spectra are computed from Eqs. (14) and (15) with $\rho_{\mu+}(0) = \sum_p \mu_+^{(p)} \rho_S(0)$ and $\rho_{\mu-}(\text{eq}) = \sum_p \mu_-^{(p)} \rho_S(\text{eq})$, respectively, and the dipole operators given by Eqs. (16) and (17).

The previously mentioned difference as regards absorption toward D₂ is even more remarkable for this numerical experiment. This is consistent with the fact that the y-polarized spectrum gives more importance to the absorption toward D₂, which amplifies the effect of the discrepancy within this higher-energy spectral range.

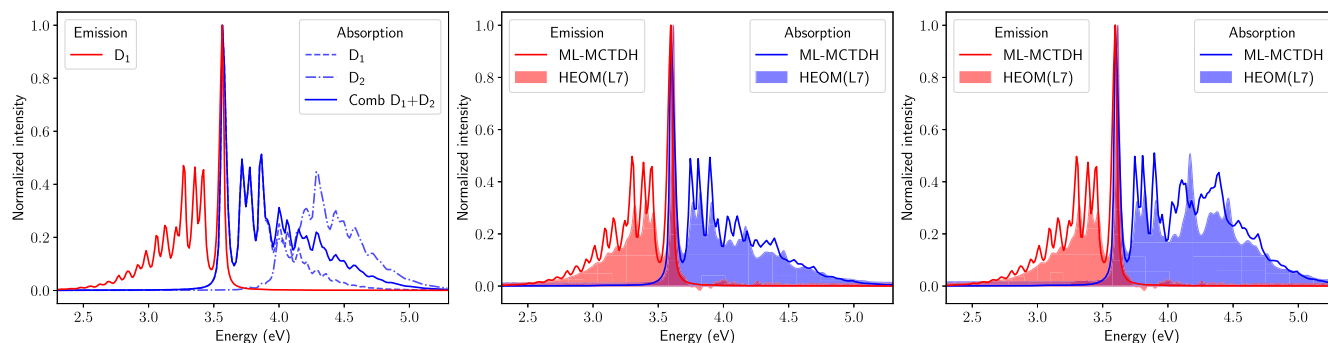


FIG. 6. Individual or combined contributions to the absorption spectra from the ground state to D_1 , D_2 , or both: blue dashed line, blue dotted line, and blue solid line, respectively. Emission spectra from the vibronic ground state within the excited (D_1 , D_2) manifold: red solid line. The ML-MCTDH spectra are broadened by using a damped autocorrelation function with damping time $\tau = 60$ fs. The HEOM spectra are displayed as filled spectra for the sake of visibility. Left: ML-MCTDH spectra for the LVC+ γ model. Center: ML-MCTDH and HEOM spectra for the LVC model with dipole strength ponderation, Eq. (30). Right: ML-MCTDH and HEOM spectra for the LVC model with a ponderation corresponding to an electric field along an oblique polarization [case $(X + Y)(X + Y)$], Eq. (31).

In both approaches, we observe that the emission spectrum exhibits no Stokes shift. Both absorption and emission spectra overlap within a marked Lorentzian-like peak at the band origin 0–0. This is typical of very fast nuclear dynamics, which is to be expected when Mukamel's $\kappa = \Lambda/\Delta$ parameter³⁰ is larger than 1, where Λ^{-1} and Δ are estimates of the bath fluctuation timescale and of the amplitude of the fluctuations, respectively. With HEOM, Λ is taken as the spectral density cutoff and $\Delta = C^{1/2}(t = 0)$ is given by the square root of the initial value of the bath correlation function.⁵³

A strict comparison of the spectra generated by ML-MCTDH or HEOM may seem somewhat disputable *per se*. Our objective is not to view such approaches as capable of competing for providing the same signal, and we did not aim at doing so from the onset. Our intention is rather to check that all such approaches, subject to their own built-in hypotheses, approximations, and limitations, can provide similar enough qualitative information as regards the overall dynamics of the system. Nevertheless, while the spectra generated with ML-MCTDH or HEOM match only qualitatively, their comparison remains much satisfactory in view of the great differences between both approaches. Each discrete mode of the LVC model is enlarged according to a uniform and quite arbitrary manner [Eq. (6)]. A more relevant simulation of the spectral densities would take the dynamics of the environment into account, as done for example in Refs. 47–49 and 73. It is possible that the interaction with a condensed phase leads to a broadening of the LVC peaks that is less pronounced than the value that we used here. Meanwhile, one should be aware that the spectral density may be drastically modified by the solvent, anyhow, as illustrated in Ref. 74. The fit of the spectral density obtained from the LVC model with three enlarged Tannor–Meier Lorentzian functions [Eq. (9)] relies on some working hypotheses, together with assuming that the tuning baths are uncorrelated. One may also invoke some explicit temperature effects since ML-MCTDH wavepackets are performed at 0 K (further broadened conveniently, according to some well-assessed procedure) and HEOM densities are typically carried out at room temperature. In the latter case, computations at low temperatures are much more demanding and require another strategy, for instance the free-pole method.^{55,57} Indeed, and as estimated in the

supplementary material, Sec. SI-V.C, Table SI-II, the computational effort is expected to be unusually heavy in the present situation.

C. Toward nonlinear spectroscopy

1. Time and frequency resolved spectra

The computation of the responses [Eq. (25) or Eq. (26)] requires a two-dimensional (t_2, t_3)-grid. The t_2 domain is chosen to probe the early nonadiabatic dynamics during 150 fs. The t_3 -range spans 300 fs. It is fixed to ensure enough decay of the correlation function before the Fourier transform. The time step is 0.24 fs (10 a.u.). A full time grid can be computed within a reasonable computational time for the 2L model only by choosing the HEOM level L7 and by discarding the Matsubara terms. The required matrices for different approximations are discussed in the supplementary material, Sec. SI-V.C, Table SI-II. Only some cuts for selected delay times t_2 have been performed in the 3L model. They are compared with the same cuts with the 2L model in the supplementary material, Fig. SI-10, to assess the validity of the approximation leading to the same qualitative information.

We first consider that the pump and the probe have the same polarization, either parallel to vector e_x (case XX) or e_y (case YY) (see Fig. 1). The polarization along an oblique direction $(e_x + e_y)/\sqrt{2}$ [case $(X + Y)(X + Y)$] is presented in the supplementary material, Fig. SI-13. Due to the transition dipole strengths, the XX case mainly populates the D_1 state, implying excitation of the p_3 branch. In contrast, in the YY case, both states are excited with nearly similar weights. The D_2 state is now significantly more populated than in the XX case and gives rise to EET toward the acceptor state D_1 .

Figure 7 presents time-and-energy-resolved spectrograms of ESE [Eq. (23)] (left panels) and TA [Eq. (22)] (right panels) for the 2L model obtained with a sampling of 9 delay times t_2 with a time step of 0.24 fs (10 a.u.) up to 2.4 fs followed by 50 values with a time step of 2.4 fs. The TA spectrograms are the sum of the ESE and GSB spectra. As discussed in Sec. II C 2, the GSB contribution does not depend on t_2 and simply adds up the absorption spectrum for the chosen polarization at all times.

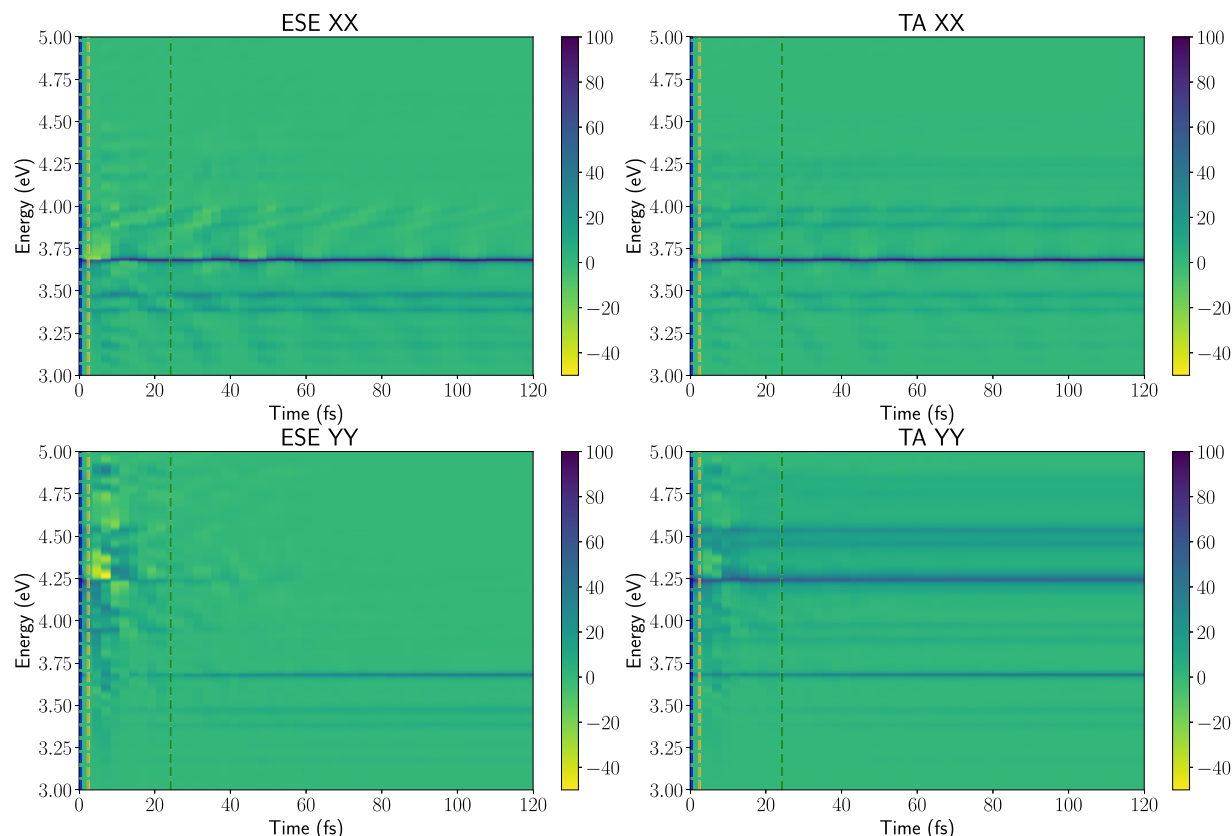


FIG. 7. Time- and frequency-resolved ESE (left panels) and TA (right panels) spectrograms [Eqs. (22) and (23)] for the approximate 2L model with only the two high-frequency peaks in the spectral densities of Fig. 2. The pump and probe are delta-like laser pulses. The polarizations of the pump and the probe are parallel—along e_x (case XX, top panels) or e_y (case YY, bottom panels). The vertical dashed lines indicate the cuts presented in Fig. 8 for the full 3L model and in the [supplementary material](#), Fig. SI-10, for the 2L model.

The ESE evolution during the early dynamics is more visible when comparing different cuts through the spectrograms for selected delays that are indicated by vertical dashed lines. The time-resolved cuts obtained for the full 3L model are shown in Fig. 8. They are given in the [supplementary material](#), Fig. SI-10, in the case of the 2L model for comparison, showing similar qualitative behavior. Cuts through the TA spectrograms are also given in the [supplementary material](#), Figs. SI-11 and SI-12, for both the 3L and 2L models.

For very short delays, ESE corresponds to the absorption spectrum. It is due to stimulated Rabi oscillations at the frequencies of the vertical transitions from the equilibrium ground state. As soon as the propagation begins, the energy gap varies and the ADOs representing the baths are gradually populated. The application of the transition dipole operators at t_2 affects all the ADOs.²³ Around $t_2 = 2.5$ fs, Fano profiles (abrupt changes from positive to negative intensities) appear due to interferences in the optical response between bath and system.^{75,76} These particular profiles are not a signature of the nonadiabatic interaction since they persist in the D_1 or D_2 states when the inter-state coupling is artificially suppressed (see the [supplementary material](#), Fig. SI-18). For a longer delay, one sees the turnover from the absorptive to the emissive profile that reaches its asymptotic value after about 125 fs.

Figure 9 illustrates the strong evolution of the ESE and TA profiles for the next-to-initial time (0.2 fs) and the long time (121 fs) close to the equilibrium. The GSB spectrum, which remains the same at all times, is drawn in dotted lines. For the very short delay, ESE and GSB are the same when the pump and probe pulses have the same polarization. The TA signal is then twice the GSB spectrum. For the long delay, the TA signal becomes equal to the GSB one in the range of the absorption spectrum since ESE becomes negligible in this domain. On the contrary, TA coincides with ESE in the range of the stationary emission spectrum. This suggests that the ESE time-dependent signal can be obtained from the time-dependent TA signal upon subtracting from it half of the initial TA spectrum, which is equivalent to the GSB contribution, at least when the polarizations are identical.

2. $S(t)$ signals as EET spectral fingerprints

Here, we illustrate how some features of the ideal impulsive pump-probe spectra may be related to EET dynamics. We first consider the evolution of some peak intensities (horizontal cuts through the spectrograms), and then, we analyze the integrated signals over the range of frequencies.

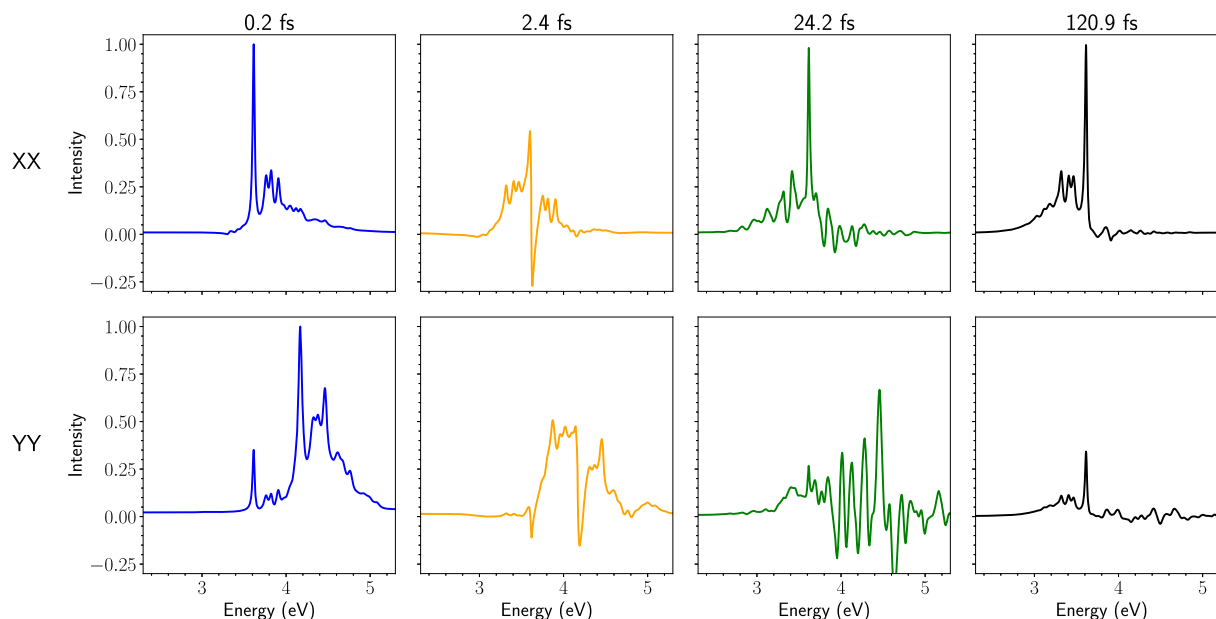


FIG. 8. Cuts through the time- and frequency-resolved ESE spectrograms for different pump–probe delays shown in dashed lines in Fig. 7 obtained in the case of the full 3L model. The corresponding cuts with the 2L model are given in the [supplementary material](#), Fig. SI-10. The polarizations are along e_x (top) and e_y (bottom). The spectra are normalized with the maximum intensity among spectra along the same line (with the same polarization).

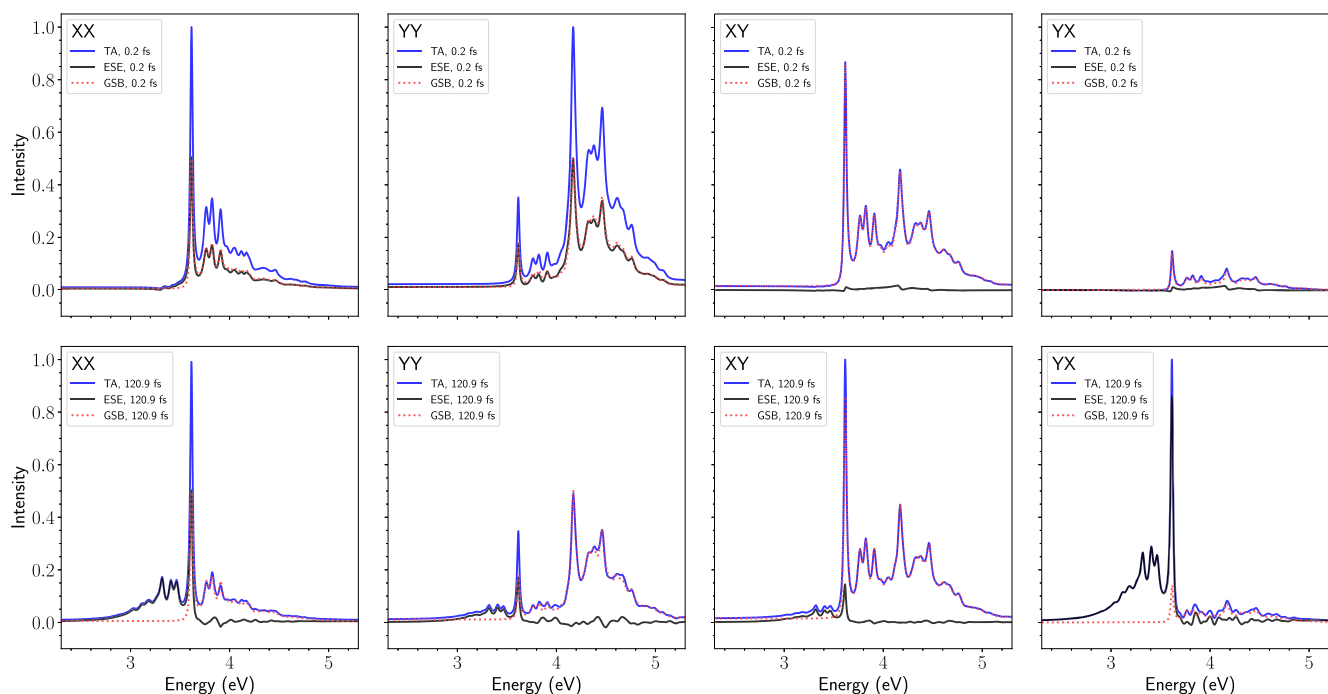


FIG. 9. ESE and TA signals obtained within the 3L model at 0.2 and 120.9 fs, compared with GSB (constant at all times). From left to right, the polarizations of the pump and the probe are parallel—along e_x (case XX, top panels) or e_y (case YY, bottom panels)—and perpendicular (crossed polarizations)—along e_x and e_y , respectively, in the case XY or vice versa in the case YX. The spectra are normalized with the maximum intensity among spectra in the same column (with the same polarization).

a. Peak evolution at relevant frequencies. Figure 10 shows the ESE intensity at two frequencies corresponding to the main transitions to state D_1 (p3 branch) or D_2 (p2 branch) at 3.681 and 4.241 eV, respectively. They are horizontal slices through the ESE spectrogram for the 2L model, but the behavior is similar to that of the 3L model as may be seen by following the maximum of the peaks in Fig. 8. When the polarization is along e_x (Fig. 10, left panel), ESE concerns the evolution in D_1 that gives rise to a negligible inter-state transition. On the contrary, a signature of EET may be seen when following the ESE for the transition at 4.241 eV with the polarization along e_y (Fig. 10, right panel). Indeed, the initial signal at 4.241 eV completely disappears in about 20 fs.

b. Integrated signals with parallel polarizations. We now examine how some fingerprint of the coherence and population evolution during the EET dynamics may be found in the integrated signal $S^{TA}(t)$ obtained upon integrating $\sigma^{TA}(\omega, t)$ [Eq. (22)] over the frequency domain. When these signals with parallel polarizations are normalized, the information is given by $S^{ESE}(t)$ [Eq. (27)] since the contribution of GSB is only a constant. $S^{ESE}(t)$ gives the time evolution of the emission spectrum area. We consider four situations, some of which are fictitious cases without inter-state coupling, in order to dissect the various influences on the signal $S^{ESE}(t)$.

- (i) Only one state, D_1 (case XX) or D_2 (case YY), is excited by approximating the transition dipoles to their largest components only ($\mu_{01} \approx (-4.77, 0, 0)$ a.u., $\mu_{02} \approx (0, 2.01, 0)$ a.u.) and assuming that there is no inter-state coupling. The initial electronic state is then stationary. Hence, the initial value $R_1(t_3 = 0, t, 0)$ does not depend on t even if the response for $t_3 \neq 0$ depends on t . Thus, $S^{ESE}(t)$ remains constant, and the shape of the ESE spectrum evolves with preserving its area. Indeed, for any delay t_2 , the density matrix remains constant with a single population $P_j = 1$ ($j = 1$ or 2). The application of μ_+ after the delay t_2 creates an optical coherence $\rho_{S,j0}$ (between the electronic system states j and 0) that is also independent of t_2 . At the end of t_3 , μ_- projects this coherent superposition into the ground state.

- (ii) The two states D_1 and D_2 are excited in the XX or YY cases [$\mu_{01} = (-4.77, 0.80, 0)$ a.u., $\mu_{02} = (1.84, 2.01, 0)$ a.u.], and the inter-state coupling is nil. The initial electronic state is then a superposition with an initial electronic coherence, but the populations remain constant. This is called a pure dephasing case of the electronic system, induced by the vibrational bath in each state. The left panel of Fig. 11 compares the evolution of $S^{ESE}(t)$ for the two polarizations XX and YY with the decoherence function of a field-free case given by the relative modulus of the electronic coherence $\tilde{C}(t) = |\rho_{S,12}(t)|/|\rho_{S,12}(0)|$. One observes that $S^{ESE}(t)$ now exhibits a fast initial decay with a rate similar to that of the (de)coherence function. $S^{ESE}(t)$ then becomes nearly constant as in the previous case when the coherence becomes negligible. In this situation, even if the populations are not varying, the electronic coherence strongly depends on the delay t_2 due to the effect of the tuning baths. The action of μ_+ at that time generates different optical coherences $\rho_{S,j0}$ ($j = 1, 2$), and the projection into the ground state after t_3 is different for each delay as long as the coherence evolves.
- (iii) Similar to case (i) but the inter-state coupling now operates. The middle panel of Fig. 11 illustrates the remarkable behavior of $S^{ESE}(t)$ that follows the evolution of the populations, in particular the decay of the most excited state. The evolution of the reduced-density matrix before the application of μ_+ is now due to the variation of the populations that are transformed to optical coherences and projected by μ_- after t_3 with a yield that evolves with the same rate as the population decay. After normalizing to disregard the value of the transition dipole, the $S^{ESE}(t)$ signal perfectly follows the population decay due to the inter-state coupling.
- (iv) Similar to case (ii) but accounting for the inter-state coupling. This is the most realistic situation. It is shown in Fig. 11, right panel. $S^{ESE}(t)$ now contains fingerprints of both the decoherence and the EET population transfer. The (de)coherence function presents a similar initial decay as in case (ii) but is damped by the population transfer. In the YY case, the most

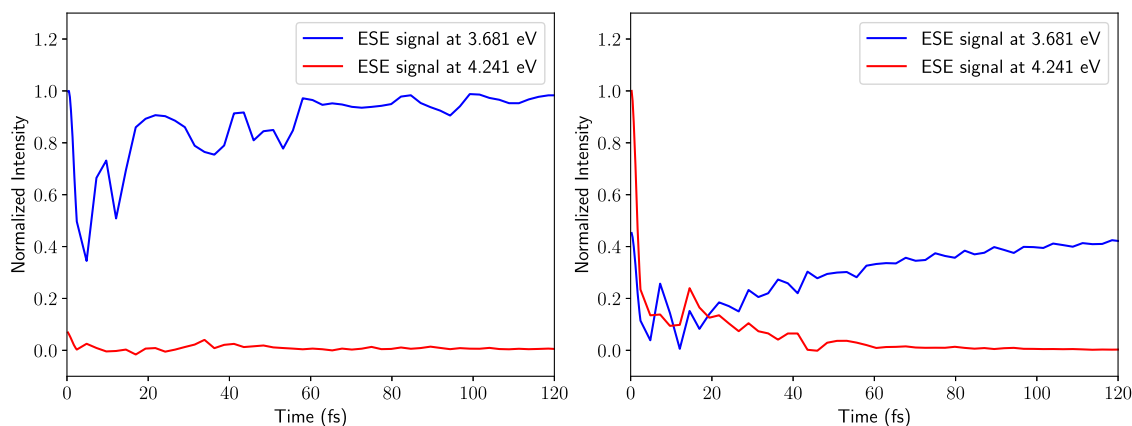


FIG. 10. Time-resolved slices through the ESE spectrogram [Eq. (23)] at two different frequencies corresponding to maxima in the steady-state absorption spectrum. Left panel: polarization along e_x ; right panel: polarization along e_y .

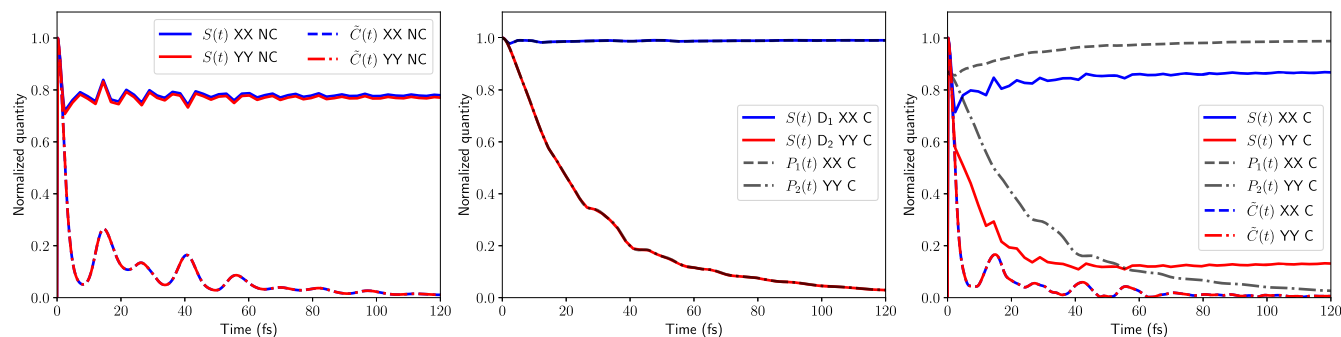


FIG. 11. Normalized integrated ESE signal, $S(t) = S^{\text{ESE}}(t)$, relative modulus of the electronic coherence, $\tilde{C}(t) = |\rho_{S,12}(t)|/|\rho_{S,12}(0)|$, and electronic populations, $P_1(t)$, $P_2(t)$, in a field-free situation (when assuming the initial preparation). From left to right: cases (ii), (iii), and (iv), such as discussed in Sec. III C 2. Case (ii): coherently superposed electronic state without inter-state coupling (NC); case (iii): single initial electronic state with inter-state coupling (C); and case (iv): coherently superposed electronic state with inter-state coupling (C). Note that (1,2)-populations are constant with time in case (ii) and the (1,2)-coherence in case (iii), which is why they are not plotted.

populated state is D_2 . Unlike the case without coupling displayed in the left panel, $S^{\text{ESE}}(t)$ now continues to decrease and the rate of decay is very similar to that of the D_2 state shown in dotted-dashed line (the initial populations, $P_1 = 0.13$ and $P_2 = 0.87$, are fixed by the normalized superposed state prepared at $t_1 = 0$). In the XX case, the behavior of $S^{\text{ESE}}(t)$ is quite similar to that without coupling, but it stabilizes to a higher value. Again, the slight increase follows the evolution of the D_1 population, shown in dashed line (the initial populations are $P_1 = 0.86$ and $P_2 = 0.14$). Hence, case (iv) is a mixture of cases (ii) and (iii) as regards the time evolution of the $S^{\text{ESE}}(t)$ signal. While it may be difficult to disentangle the two effects in practice, our numerical experiments thus provide a guideline for deciphering the relative roles played by decoherence and EET when probing the time-resolved spectroscopy of an optically active manifold of two vibronically coupled excited electronic states that can be excited coherently by the

pump. For the sake of completion, non-normalized signals are provided in the [supplementary material](#), Fig. SI-17.

c. Anisotropy decay signal. Up to now, we extensively discussed the integrated signals of ESE for parallel polarizations of the pump and probe pulses, $S_{XX}^{\text{ESE}}(t)$ or $S_{YY}^{\text{ESE}}(t)$. Similar integrated signals can be obtained for perpendicular polarizations, $S_{XY}^{\text{ESE}}(t)$ or $S_{YX}^{\text{ESE}}(t)$. More importantly, these integrated signals can be evaluated for TA upon considering $S_{XX}^{\text{TA}}(t)$ and $S_{XY}^{\text{TA}}(t)$, or $S_{YY}^{\text{TA}}(t)$ and $S_{YX}^{\text{TA}}(t)$, which allows for the calculation of the isotropic signal, $\Delta S_{\text{iso}}(t)$ [Eq. (29)], and the anisotropy decay signal, $r(t)$ [Eq. (28)]. Such signals are shown in Fig. 12 and compared for the pump-probe setups with parallel XX and perpendicular (crossed) polarizations XY (blue lines) or with YY and YX (red lines).

Exciting with polarization along e_x mainly populates the D_1 state, while both excited states are reached with exciting polarization along e_y . The very fast variation of $r(t)$ in that case reveals

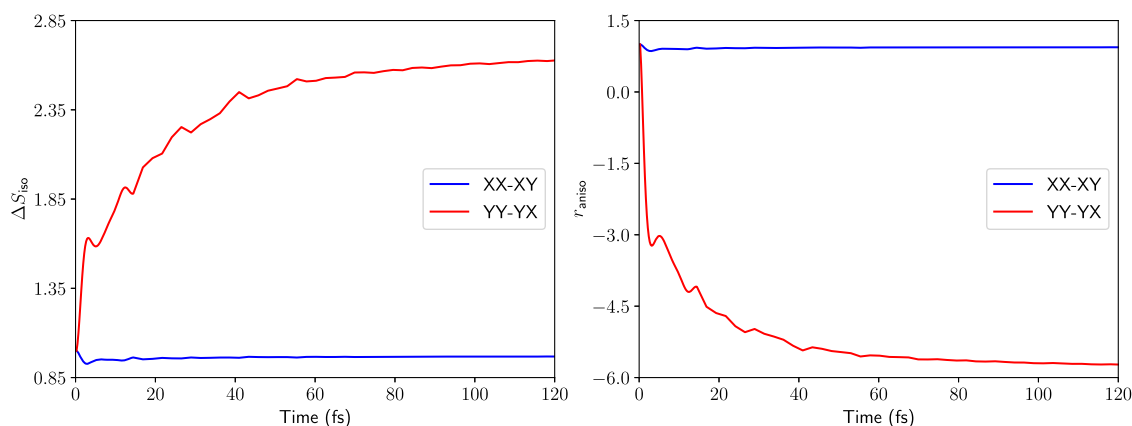


FIG. 12. Signals with parallel and perpendicular polarizations when exciting with polarization along e_x (case XX-XY) or polarization along e_y (case YY-YX). Left panel: $\Delta S_{\text{iso}}(t)$ [Eq. (29)]; right panel: $r(t)$ [Eq. (28)].

the EET toward the acceptor state, leading to a fast change of the polarization. The change of polarization is completed in about 40 fs, as expected from the different intermediate signals discussed above. Indeed, when the pump is polarized along e_y , the spectrogram $\sigma^{\text{ESE}}(\omega, t)$, the integrated signal $S^{\text{ESE}}(t)$, and finally the anisotropic decay signal $r(t)$ all contain the same signature of the ultrafast transfer from the D_2 to the D_1 state. In this context, we expect these experimentally observable signals to characterize the timescale and the yield of the electronic population transfer. We note that the occurrence of weak oscillations in both $\Delta S_{\text{iso}}(t)$ and $r(t)$ is a fingerprint of the vibronic coherence as already observed in Fig. 11 (right panel).

3. 2D spectra

Figure 13 shows the 2D spectra for two population times t_2 with parallel or crossed polarizations computed with the 2L model. The grids of the coherence time t_1 and the detection time t_3 extend over 100 and 300 fs, respectively, to ensure the decay of the corresponding correlation functions. For the ultra-short waiting time $t_2 = 0.24$ fs, the position of the diagonal peaks in the cases XX and YY matches the absorption or the early emission spectra at the Franck–Condon geometry (see the [supplementary material](#), Fig. SI-10).

Indeed, for very short population times, the GSB and ESE contributions are the same. In the XX case, the intense peak at 3.69 eV and the two peaks at 3.90 and 3.99 eV are transitions toward the D_1 state reached by the high $\mu_{01,x}$ component. With the polarization along e_y (case YY), the optical coherences toward the D_1 and

D_2 states are of the same order of magnitude. The first three diagonal peaks coincide with those obtained in the XX case with a lower intensity due to the lower value of the transition dipole $\mu_{01,y}$ toward this D_1 state (see Fig. 1). The following diagonal peaks give the vibronic progression corresponding to the D_2 state at 4.43, 4.53, 4.75, and 4.80 eV. The off-diagonal peaks confirm the possible EET from the D_2 state toward the acceptor state, for instance an excitation at 4.25 eV is likely to give a signal at 3.69 eV. This effect of probing EET is more obvious when using the crossed-polarization XY case. The lower off-diagonal peak linking excitation at 4.25 eV and detection at 3.69 eV from the D_1 state is very intense. The other following peaks resulting from excitation at 4.25 eV correspond to the detection of the states at 3.90 and 3.99 eV also belonging to the acceptor state.

For a longer waiting time $t_2 = 48.2$ fs, even if the GSB remains the same, the ESE contribution does not match the Franck–Condon region anymore and nearly coincides with the asymptotic emission of the relaxed system. In the XX case, at an excitation energy of 3.69 eV, one observes the two weak emission peaks at 3.4 and 3.49 eV (see the [supplementary material](#), Fig. SI-10). The intensity of all the peaks in the YY case is lower than for the short waiting time, confirming the fast population decay from the D_2 state. The cross-peak at 4.25 and 3.69 eV reveals the excitation in D_2 and detection from the acceptor state. In a similar way, the two weak detection peaks at 4.25 and 3.4 eV and 4.25 and 3.49 eV are also a signature of the transfer toward the D_1 state. With the other crossed polarization YX, the diagonal peaks related to the Franck–Condon excitation disappear as in the previous case. The main peak at 4.25 and 3.69 eV

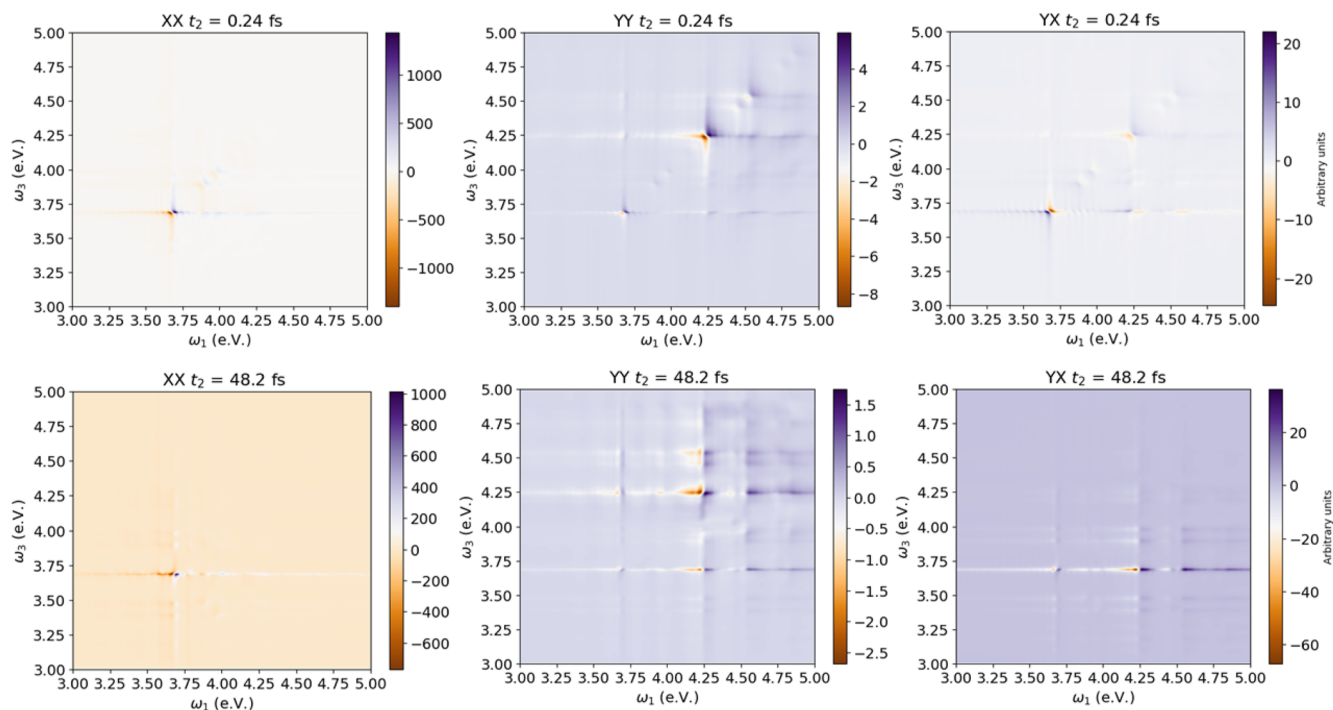


FIG. 13. 2D spectra for two population times t_2 obtained with parallel polarizations along e_x (case XX) or e_y (case YY) and crossed polarizations (case YX).

and the satellite ones (4.25 and 3.4 eV and 4.25 and 3.49 eV) confirm the presence of EET. The difference of the intensity when detecting with polarization Y or X comes from the difference of the components of the transition dipoles, which occur at power four in 2D spectra.

IV. CONCLUSIONS AND OUTLOOK

The first focus of the present work was to extend to high dimensionality and/or dissipative approaches our previous reduced-dimensionality study of ultrafast EET occurring in the smallest asymmetrical *meta*-substituted PPE oligomer, m23, made of 2-ring (p2) and 3-ring (p3) *para*-substituted pseudo-fragments.¹¹

As regards this prototypical system, the donor state is mainly localized on p2 and the acceptor state on p3. For the isolated m23 system, we have constructed an *ab initio* high-dimensional vibronic coupling Hamiltonian (VCH) model for the first two singlet electronic excited states accounting for all the 93 in-plane vibrational degrees of freedom in terms of a linear vibronic coupling (LVC) model and various types of quadratic vibronic coupling (QVC) extensions.

Wavepacket simulations using a 93-dimensional ML-MCTDH approach confirmed a typical timescale of about 25 fs for intramolecular EET, which was confirmed with the dissipative reduced-density approach known as HEOM. The primary role of the high-frequency acetylenic and quinoidal vibrations was confirmed.

The second focus of our work was to investigate the nonlinear spectroscopy of m23 with particular attention paid to time-dependent TA spectra as regards their GSB and ESE components and 2D spectroscopy, upon deciphering the respective roles of the different polarizations. Our primary intention here was not to improve an already-present method with new features, but rather to show how to take benefit of approaches developed by different communities to get a pragmatical recipe/strategy aimed at addressing a realistic situation: a molecule of decent size, of much experimental 2D-spectroscopic interest for EET, which also occurs to cause challenging numerical problems as opposed to better-behaved toy models, and that will eventually be subject to some approximations. The time-dependent spectra and the 2D spectra of the m23 dimer have recently raised interest and been computed with a semi-classical approach. Hence, we believe that it remains interesting to probe the possibilities and the limits of the HEOM approach for such a complex and interesting system for EET.

Highlighting the role of the high-frequency modes allowed us to retain only the essential parts of the spectral densities and generate spectrograms, which deserve some care so as not to become too computationally expensive. However, we also showed that low-cost simulations of integrated signals is possible in the delta-like pulse approximation upon using the response function at $t_3 = 0$ instead of integrating the spectra.

All the nonlinear spectra presented here correspond to ideal impulsive delta-like laser pulses, and some fingerprints of EET have been characterized in this context. This illustrates that a minimal model deserves the essential description of the EET process as a complement to different approaches with more realistic pulses and more electronic states.^{14,15} Further investigations, on both the

theoretical and experimental fronts, are awaited, for instance to take into account the solvent effect.

Even if nonlinear signals were only computed with HEOM in this work, there is no *a priori* limitation in getting the same signals with (ML-)MCTDH, but we purposefully did not aim at following such avenues in the present work, since we wanted to focus on the HEOM approach. Such wavepacket protocols have been recently proposed by other authors according to the time-dependent Davydov method⁷⁰ or in Refs. 35 and 77, where the time-resolved signals directly depend on the overlaps of the nuclear wavepackets propagated with standard MCTDH. Some practical complications may arise from the use of ML-MCTDH wavepackets for such a large-dimensional system, as opposed to standard MCTDH with a dimensionally reduced model. Along the same line, we expect 2DES line shapes to be accessible within the same framework, only with more extensive computational resources and clever-crafted input/output data management. This is left for further work.

SUPPLEMENTARY MATERIAL

The [supplementary material](#) includes the following: a discussion on bilinear terms in the VCH models, a representation of the ML-MCTDH wavefunction, additional information on nuclear displacements and on spectral densities, operational equations for HEOM, examples of bath dynamics in HEOM, comparisons of the population dynamics in the 2L or 3L models, expressions of the nonlinear responses, and additional figures for the discussion of nonlinear spectroscopy.

ACKNOWLEDGMENTS

J.G. acknowledges the French MESR (Ministère chargé de l'Enseignement Supérieur et de la Recherche) and the ENS (Ecole Normale Supérieure) of Lyon for funding his Ph.D. grant, hosted at the University of Montpellier. We thank J.M. Teuler of the University Paris-Saclay for the upgrade of his JMFFFT-7.2 library (CNRS-IDRIS France).

AUTHOR DECLARATIONS

Conflict of Interest

The authors have no conflicts to disclose.

Author Contributions

Joachim Galiana: Investigation (equal); Methodology (equal); Supervision (lead); Visualization (lead); Writing – original draft (equal); Writing – review & editing (equal). **Michèle Desouter-Lecomte:** Investigation (equal); Methodology (equal); Software (lead); Writing – original draft (equal); Writing – review & editing (equal). **Benjamin Lasorne:** Investigation (supporting); Methodology (equal); Supervision (lead); Visualization (lead); Writing – original draft (supporting); Writing – review & editing (equal).

DATA AVAILABILITY

The data that support the findings of this study are available from the corresponding author upon reasonable request.

REFERENCES

- ¹Z. Xu and J. S. Moore, "Design and synthesis of a convergent and directional molecular antenna," *Acta Polym.* **45**, 83–87 (1994).
- ²C. Devadoss, P. Bharathi, and J. S. Moore, "Energy transfer in dendritic macromolecules: Molecular size effects and the role of an energy gradient," *J. Am. Chem. Soc.* **118**, 9635–9644 (1996).
- ³M. R. Shortreed, S. F. Swallen, Z.-Y. Shi, W. Tan, Z. Xu *et al.*, "Directed energy transfer funnels in dendrimeric antenna supermolecules," *J. Phys. Chem. B* **101**, 6318–6322 (1997).
- ⁴J. S. Melinger, Y. Pan, V. D. Kleiman, Z. Peng, B. L. Davis, D. McMorro, and M. Lu, "Optical and photophysical properties of light-harvesting phenylacetylene monodendrons based on unsymmetrical branching," *J. Am. Chem. Soc.* **124**, 12002–12012 (2002).
- ⁵S. F. Swallen, R. Kopelman, J. S. Moore, and C. Devadoss, "Dendrimer photoantenna supermolecules: Energetic funnels, exciton hopping and correlated excimer formation," *J. Mol. Struct.* **485–486**, 585–597 (1999).
- ⁶R. Kopelman, M. Shortreed, Z.-Y. Shi, W. Tan, Z. Xu *et al.*, "Spectroscopic evidence for excitonic localization in fractal antenna supermolecules," *Phys. Rev. Lett.* **78**, 1239–1242 (1997).
- ⁷T. Minami, S. Tretiak, V. Chernyak, and S. Mukamel, "Frenkel-exciton Hamiltonian for dendrimeric nanostar," *J. Lumin.* **87–89**, 115–118 (2000).
- ⁸V. Chernyak, T. Minami, and S. Mukamel, "Exciton transport in molecular aggregates probed by time and frequency gated optical spectroscopy," *J. Chem. Phys.* **112**, 7953–7963 (2000).
- ⁹S. Fernandez-Alberti, V. D. Kleiman, S. Tretiak, and A. E. Roitberg, "Nonadiabatic molecular dynamics simulations of the energy transfer between building blocks in a phenylene ethynylene dendrimer," *J. Phys. Chem. A* **113**, 7535–7542 (2009).
- ¹⁰J. Huang, L. Du, D. Hu, and Z. Lan, "Theoretical analysis of excited states and energy transfer mechanism in conjugated dendrimers," *J. Comput. Chem.* **36**, 151–163 (2015).
- ¹¹J. Galiana and B. Lasorne, "Excitation energy transfer and vibronic relaxation through light-harvesting dendrimer building blocks: A nonadiabatic perspective," *J. Chem. Phys.* **160**, 104104 (2024).
- ¹²W. Malone, B. Nebgen, A. White, Y. Zhang, H. Song *et al.*, "NEXMD software package for nonadiabatic excited state molecular dynamics simulations," *J. Chem. Theory Comput.* **16**, 5771–5783 (2020).
- ¹³S. Fernandez-Alberti, D. V. Makhov, S. Tretiak, and D. V. Shalashilin, "Non-adiabatic excited state molecular dynamics of phenylene ethynylene dendrimer using a multiconfigurational Ehrenfest approach," *Phys. Chem. Chem. Phys.* **18**, 10028–10040 (2016).
- ¹⁴D. Hu, J. Peng, L. Chen, M. F. Gelin, and Z. Lan, "Spectral fingerprint of excited-state energy transfer in dendrimers through polarization-sensitive transient-absorption pump-probe signals: On-the-fly nonadiabatic dynamics simulations," *J. Phys. Chem. Lett.* **12**, 9710–9719 (2021).
- ¹⁵J. Zhang, J. Peng, D. Hu, M. F. Gelin, and Z. Lan, "What two-dimensional electronic spectroscopy can tell us about energy transfer in dendrimers: Ab initio simulations," *J. Phys. Chem. Lett.* **16**, 1007–1015 (2025).
- ¹⁶H. D. Meyer, U. Manthe, and L. S. Cederbaum, "The multi-configurational time-dependent Hartree approach," *Chem. Phys. Lett.* **165**, 73–78 (1990).
- ¹⁷M. Beck, A. Jäckle, G. A. Worth, and H. D. Meyer, "The multiconfiguration time-dependent Hartree (MCTDH) method: A highly efficient algorithm for propagating wavepackets," *Phys. Rep.* **324**, 1–105 (2000).
- ¹⁸S. Liu, J. Peng, P. Bao, Q. Shi, and Z. Lan, "Ultrafast excited-state energy transfer in phenylene ethynylene dendrimer: Quantum dynamics with the tensor network method," *J. Phys. Chem. A* **128**, 6337–6350 (2024).
- ¹⁹H. Wang and M. Thoss, "Multilayer formulation of the multiconfiguration time-dependent Hartree theory," *J. Chem. Phys.* **119**, 1289–1299 (2003).
- ²⁰U. Manthe, "A multilayer multiconfigurational time-dependent Hartree approach for quantum dynamics on general potential energy surfaces," *J. Chem. Phys.* **128**, 164116 (2008).
- ²¹H. Wang, "Multilayer multiconfiguration time-dependent Hartree theory," *J. Phys. Chem. A* **119**, 7951–7965 (2015).
- ²²Y. Tanimura and R. Kubo, "Time evolution of a quantum system in contact with a nearly Gaussian-Markoffian noise bath," *J. Phys. Soc. Jpn.* **58**, 101–114 (1989).
- ²³Y. Tanimura, "Stochastic Liouville, Langevin, Fokker-Planck, and master equation approaches to quantum dissipative systems," *J. Phys. Soc. Jpn.* **75**, 082001 (2006).
- ²⁴Y. Tanimura, "Numerically 'exact' approach to open quantum dynamics: The hierarchical equations of motion (heom)," *J. Chem. Phys.* **153**, 020901 (2020).
- ²⁵R.-X. Xu and Y. Yan, "Dynamics of quantum dissipation systems interacting with bosonic canonical bath: Hierarchical equations of motion approach," *Phys. Rev. E* **75**, 031107 (2007).
- ²⁶Q. Shi, L. Chen, G. Nan, R.-X. Xu, and Y. Yan, "Efficient hierarchical Liouville space propagator to quantum dissipative dynamics," *J. Chem. Phys.* **130**, 084105 (2009).
- ²⁷S. Bai, S. Zhang, C. Huang, and Q. Shi, "Hierarchical equations of motion for quantum chemical dynamics: Recent methodology developments and applications," *Acc. Chem. Res.* **57**, 3151–3160 (2024).
- ²⁸E. J. Heller, "Time-dependent approach to semiclassical dynamics," *J. Chem. Phys.* **62**, 1544–1555 (1975).
- ²⁹M. Cho, N. F. Scherer, G. R. Fleming, and S. Mukamel, "Photon echoes and related four-wave-mixing spectroscopies using phase-locked pulses," *J. Chem. Phys.* **96**, 5618–5629 (1992).
- ³⁰S. Mukamel, *Principles of Nonlinear Optical Spectroscopy* (Oxford University Press, 1995).
- ³¹M. Kowalewski, B. P. Fingerhut, K. E. Dorfman, K. Bennett, and S. Mukamel, "Simulating coherent multidimensional spectroscopy of nonadiabatic molecular processes: From the infrared to the x-ray regime," *Chem. Rev.* **117**, 12165–12226 (2017).
- ³²R. Borrego-Varillas, A. Nenov, L. Ganzer, A. Oriana, C. Manzoni *et al.*, "Two-dimensional UV spectroscopy: A new insight into the structure and dynamics of biomolecules," *Chem. Sci.* **10**, 9907–9921 (2019).
- ³³E. Collini, "2D electronic spectroscopic techniques for quantum technology applications," *J. Phys. Chem. C* **125**, 13096–13108 (2021).
- ³⁴P. A. Rose and J. J. Krich, "Automatic Feynman diagram generation for nonlinear optical spectroscopies and application to fifth-order spectroscopy with pulse overlaps," *J. Chem. Phys.* **154**, 034109 (2021).
- ³⁵F. Segatta, D. Aranda, F. Aleotti, F. Montorsi, S. Mukamel *et al.*, "Time-resolved X-ray absorption spectroscopy: An MCTDH quantum dynamics protocol," *J. Chem. Theory Comput.* **20**(1), 307–322 (2024).
- ³⁶S. A. Shah, H. Li, E. R. Bittner, C. Silva, and A. Piryatinski, "QuDPy: A python-based tool for computing ultrafast non-linear optical responses," *Comput. Phys. Commun.* **292**, 108891 (2023).
- ³⁷M. J. Frisch, G. W. Trucks, H. B. Schlegel, G. E. Scuseria, M. A. Robb *et al.*, *Gaussian 16, Revision A.03*, Gaussian, Inc., Wallingford, CT, 2016.
- ³⁸G. Breuil, T. Etienne, and B. Lasorne, "Bright-to-dark-to-bright photoisomerization in a forked (phenylene ethynylene) dendrimer prototype and its building blocks: A new mechanistic shortcut for excitation-energy transfer?," *Eur. Phys. J.: Spec. Top.* **232**, 2101–2115 (2023).
- ³⁹E. K. L. Ho and B. Lasorne, "Diabatic pseudofragmentation and nonadiabatic excitation-energy transfer in meta-substituted dendrimer building blocks," *Comput. Theor. Chem.* **1156**, 25–36 (2019).
- ⁴⁰S. Fernandez-Alberti, V. D. Kleiman, S. Tretiak, and A. E. Roitberg, "Unidirectional energy transfer in conjugated molecules: The crucial role of high-frequency C≡C bonds," *J. Phys. Chem. Lett.* **1**, 2699–2704 (2010).
- ⁴¹J. Galiana and B. Lasorne, "On the unusual Stokes shift in the smallest PPE dendrimer building block: Role of the vibronic symmetry on the band origin?," *J. Chem. Phys.* **158**, 124113 (2023).
- ⁴²B. Gonon, B. Lasorne, G. Karras, L. Joubert-Doriol, D. Lauvergnat *et al.*, "A generalized vibronic-coupling Hamiltonian for molecules without symmetry: Application to the photoisomerization of benzopyran," *J. Chem. Phys.* **150**, 124109 (2019).

- ⁴³B. Gonon, A. Perveaux, F. Gatti, D. Lauvergnat, and B. Lasorne, "On the applicability of a wavefunction-free, energy-based procedure for generating first-order non-adiabatic couplings around conical intersections," *J. Chem. Phys.* **147**, 114114 (2017).
- ⁴⁴H.-P. Breuer and F. Petruccione, *The Theory of Open Quantum Systems* (Oxford University Press, 2002).
- ⁴⁵U. Weiss, *Quantum Dissipative Systems* (World Scientific, Singapore, 2012).
- ⁴⁶V. May and O. Kühn, *Charge and Energy Transfer Dynamics in Molecular Systems* (John Wiley & Sons, Inc., 2011).
- ⁴⁷E. Mangaud, A. de la Lande, C. Meier, and M. Desouter-Lecomte, "Electron transfer within a reaction path model calibrated by constrained DFT calculations: Application to mixed-valence organic compounds," *Phys. Chem. Chem. Phys.* **17**, 30889–30903 (2015).
- ⁴⁸Z. Tong, X. Gao, M. S. Cheung, B. D. Dunietz, E. Geva, and X. Sun, "Charge transfer rate constants for the carotenoid-porphyrin- C_{60} molecular triad dissolved in tetrahydrofuran: The spin-boson model vs the linearized semiclassical approximation," *J. Chem. Phys.* **153**, 044105 (2020).
- ⁴⁹A. J. Dunnett, D. Gowland, C. M. Isborn, A. W. Chin, and T. J. Zuehlsdorff, "Influence of non-adiabatic effects on linear absorption spectra in the condensed phase: Methylene blue," *J. Chem. Phys.* **155**, 144112 (2021).
- ⁵⁰R. Martinazzo, K. H. Hughes, F. Martelli, and I. Burghardt, "Effective spectral densities for system-environment dynamics at conical intersections: S2-S1 conical intersection in pyrazine," *Chem. Phys.* **377**, 21–29 (2010).
- ⁵¹H. Tamura, R. Martinazzo, M. Ruckebauer, and I. Burghardt, "Quantum dynamics of ultrafast charge transfer at an oligothiophene-fullerene heterojunction," *J. Chem. Phys.* **137**, 22A540 (2012).
- ⁵²G. A. Worth, K. Giri, G. W. Richings, I. Burghardt, M. H. Beck, A. Jäckle, and H. D. Meyer, *The Quantics Package, Version 2.0*, University of Birmingham, Birmingham, UK, 2020.
- ⁵³E. Mangaud, A. Jaouadi, A. Chin, and M. Desouter-Lecomte, "Survey of the hierarchical equations of motion in tensor-train format for non-Markovian quantum dynamics," *Eur. Phys. J.: Spec. Top.* **232**, 1847–1869 (2023).
- ⁵⁴A. Pomyalov, C. Meier, and D. J. Tannor, "The importance of initial correlations in rate dynamics: A consistent non-markovian master equation approach," *Chem. Phys.* **370**, 98–108 (2010).
- ⁵⁵B. Le Dé, A. Jaouadi, E. Mangaud, A. W. Chin, and M. Desouter-Lecomte, "Managing temperature in open quantum systems strongly coupled with structured environments," *J. Chem. Phys.* **160**, 244102 (2024).
- ⁵⁶C. Meier and D. J. Tannor, "Non-Markovian evolution of the density operator in the presence of strong laser fields," *J. Chem. Phys.* **111**, 3365–3376 (1999).
- ⁵⁷M. Xu, Y. Yan, Q. Shi, J. Ankerhold, and J. T. Stockburger, "Taming quantum noise for efficient low temperature simulations of open quantum systems," *Phys. Rev. Lett.* **129**, 230601 (2022).
- ⁵⁸H. Liu, L. Zhu, S. Bai, and Q. Shi, "Reduced quantum dynamics with arbitrary bath spectral densities: Hierarchical equations of motion based on several different bath decomposition schemes," *J. Chem. Phys.* **140**, 134106 (2014).
- ⁵⁹A. Ishizaki and Y. Tanimura, "Multidimensional vibrational spectroscopy for tunneling processes in a dissipative environment," *J. Chem. Phys.* **123**, 014503 (2005).
- ⁶⁰Y. Tanimura, "Reduced hierarchy equations of motion approach with Drude plus Brownian spectral distribution: Probing electron transfer processes by means of two-dimensional correlation spectroscopy," *J. Chem. Phys.* **137**, 22A550 (2012).
- ⁶¹L. Chen, R. Zheng, Q. Shi, and Y. Yan, "Two-dimensional electronic spectra from the hierarchical equations of motion method: Application to model dimers," *J. Chem. Phys.* **132**, 024505 (2010).
- ⁶²K.-B. Zhu, R.-X. Xu, H. Y. Zhang, J. Hu, and Y. J. Yan, "Hierarchical dynamics of correlated system-environment coherence and optical spectroscopy," *J. Phys. Chem. B* **115**, 5678–5684 (2011).
- ⁶³L. Chen, R. Zheng, Y. Jing, and Q. Shi, "Simulation of the two-dimensional electronic spectra of the Fenna-Matthews-Olson complex using the hierarchical equations of motion method," *J. Chem. Phys.* **134**, 194508 (2011).
- ⁶⁴Y. Yan, Y. Liu, T. Xing, and Q. Shi, "Theoretical study of excitation energy transfer and nonlinear spectroscopy of photosynthetic light-harvesting complexes using the nonperturbative reduced dynamics method," *Wiley Interdiscip. Rev.: Comput. Mol. Sci.* **11**, e1498 (2021).
- ⁶⁵J. H. Fetherolf and T. C. Berkelbach, "Linear and nonlinear spectroscopy from quantum master equations," *J. Chem. Phys.* **147**, 244109 (2017).
- ⁶⁶M. Khalil, N. Demirdöven, and A. Tokmakoff, "Coherent 2D IR spectroscopy: Molecular structure and dynamics in solution," *J. Phys. Chem. A* **107**, 5258–5279 (2003).
- ⁶⁷D. Abramavicius, B. Palmieri, D. V. Voronine, F. Šanda, and S. Mukamel, "Coherent multidimensional optical spectroscopy of excitons in molecular aggregates: quasiparticle versus supermolecule perspectives," *Chem. Rev.* **109**, 2350–2408 (2009).
- ⁶⁸V. Butkus, D. Zigmantas, L. Valkunas, and D. Abramavicius, "Vibrational vs. electronic coherences in 2D spectrum of molecular systems," *Chem. Phys. Lett.* **545**, 40–43 (2012).
- ⁶⁹J. Krčmář, M. F. Gelin, and W. Domcke, "Simulation of femtosecond two-dimensional electronic spectra of conical intersections," *J. Chem. Phys.* **143**, 074308 (2015).
- ⁷⁰K. Sun, Z. Huang, M. F. Gelin, L. Chen, and Y. Zhao, "Monitoring of singlet fission via two-dimensional photon-echo and transient-absorption spectroscopy: Simulations by multiple Davydov trial states," *J. Chem. Phys.* **151**, 114102 (2019).
- ⁷¹T. Joo, Y. Jia, J.-Y. Yu, M. J. Lang, and G. R. Fleming, "Third-order nonlinear time domain probes of solvation dynamics," *J. Chem. Phys.* **104**, 6089–6108 (1996).
- ⁷²S. Bai, K. Song, and Q. Shi, "Effects of different quantum coherence on the pump-probe polarization anisotropy of photosynthetic light-harvesting complexes: A computational study," *J. Phys. Chem. Lett.* **6**(10), 1954–1960 (2015).
- ⁷³E. Lambertson, D. Bashirova, K. E. Hunter, B. Hansen, and T. J. Zuehlsdorff, "Computing linear optical spectra in the presence of nonadiabatic effects on graphics processing units using molecular dynamics and tensor-network approaches," *J. Chem. Phys.* **161**, 114101 (2024).
- ⁷⁴K. E. Hunter, Y. Mao, A. W. Chin, and T. J. Zuehlsdorff, "Environmentally driven symmetry breaking quenches dual fluorescence in proflavine," *J. Phys. Chem. Lett.* **15**, 4623–4632 (2024).
- ⁷⁵H.-D. Zhang and Y. Yan, "Onsets of hierarchy truncation and self-consistent Born approximation with quantum mechanics prescriptions invariance," *J. Chem. Phys.* **143**, 214112 (2015).
- ⁷⁶D. Finkelstein-Shapiro, F. Poulsen, T. Pullerits, and T. Hansen, "Coherent two-dimensional spectroscopy of a fano model," *Phys. Rev. B* **94**, 205137 (2016).
- ⁷⁷F. Segatta, D. A. Ruiz, F. Aleotti, M. Yaghoubi, S. Mukamel *et al.*, "Nonlinear molecular electronic spectroscopy via MCTDH quantum dynamics: From exact to approximate expressions," *J. Chem. Theory Comput.* **19**, 2075–2091 (2023).